Received: 30 March 2022 | Revised: 12 August 2022 | Accepted: 26 September 2022

IET Renewable Power Generation

DOI: 10.1049/rpg2.12616

The Institution of Engineering and Technology WILEY

ORIGINAL RESEARCH

# Power system stability improvement considering drive train oscillations of virtual synchronous generator-regulated type-4 wind turbines

**Seyed Saeied Heidari Yazdi**[1] | **Yaser Shokri-Kalandaragh**[2] | **Mehdi Bagheri**[1]

[1]Department of Electrical and Computer Engineering, Nazarbayev University, Astana, Kazakhstan

[2]Department of Advanced Technologies, University of Mohaghegh Ardabili, Namin, Iran

**Correspondence**
Mehdi Bagheri, Department of Electrical and Computer Engineering, Nazarbayev University, Astana, Kazakhstan
Email: mehdi.bagheri@nu.edu.kz

**Funding information**
Collaborative Research Grant (CRP) of Nazarbayev University, Grant/Award Number: 021220CRP0322

**Abstract**

The type-4 wind turbine generators (WTGs) can provide inertial frequency response by implementing the virtual synchronous generator (VSG) concept. However, unstable torsional oscillations (TOs) would be induced in the multi-mass-spring drive-train which can destabilize the entire power system. In this study, participation factor analyses are performed for a power system inclusive of a thermal unit and aggregated WTG system. The system's eigenvalues are characterized and the possible detrimental impacts of TOs on the inertia provision process and overall power system stability are demonstrated and the related stability limits are identified. A comprehensive active torsional oscillations damper (CA-TOD) and a supercapacitor-based energy storage system (ESS) are presented and discussed to implement the CA-TOD. A state of charge (SoC) regulator is also employed to set the reference speed difference for the turbine-generator. Small-signal studies and electro-magnetic transient (EMT) simulations are performed to evaluate the functionality of the CA-TOD and SoC controller and estimate their impacts on the system's dynamics. The robust performance of the CA-TOD is compared to the band-pass filter-based TOD by sweeping key control parameters of the VSG and emulating drive-train parameter uncertainty. Key results are cross-verified by EMT simulations of a multimachine power system.

## 1 | INTRODUCTION

### 1.1 | Problem statement

Recent grid codes require wind turbine generators (WTGs) to provide inertial frequency response to support the stability of the power system frequency; hence, novel frequency regulation schemes have been designed [1–4]. Among the schemes, the virtual synchronous generator (VSG) concept is more feasible as it can properly connect to a weak AC grid, has grid forming ability, and provides natural frequency support and harmonious grid integration [5].

The inertial frequency support can be performed using WTG's stored kinetic energy; however, it may raise a serious concern regarding the internal stability of multi-poles and direct-drive type-4 WTGs [6]. The low stiffness of the drive-train's shaft, due to the high number of pole pairs, and the absence of inherent damping torque, due to lack of damper windings and field-oriented controllers, are the main issues in this concern [7–9]. There will be torsional oscillations in the frequency range of [0.1–10] Hz for the generator's speed and the torque/angle of the drive-train's shaft. The WTG system can be regarded as a non-linear dynamic system whose inputs include wind speed and voltage and frequency of the power system. In this sense, torsional oscillations would be triggered and reflected on the WTG's state variables by the change of its inputs [8]. The frequency of torsional oscillations coincides with the frequency range of the power system's inter-area oscillations [0.1–2.5] Hz [8, 10]. Since these oscillations might be reflected at the WTG's output power, the power system may become unstable. Therefore, comprehensive studies should be conducted to study the dynamics of the power systems penetrated by the

frequency responsive type-4 WTGs and to stabilize the emerged torsional oscillations.

## 1.2 | Literature review

The control structure of type-4 WTGs can be classified according to the converter in charge of the DC voltage control [6]:

- First structure of DC voltage control: Grid side converter (GSC) regulates the DC voltage and machine side converter (MSC) enforces the maximum power point tracking (MPPT).
- Second structure of DC voltage control: MSC controls the DC voltage and GSC applies the adopted MPPT concept.

The characteristics of WTG's internal dynamics and torsional oscillations and mechanism of propagation of oscillations into the power system are different in these two control structures. Present studies mainly tried stabilizing WTG's torsional oscillations in non-frequency responsive WTGs when wind speed fluctuates.

In the first structure of DC voltage control, the MPPT process is usually obtained through implementing the curve of optimal power/torque reference versus the generator's speed in the control software of MSC. This curve also acts as an effective active torsional oscillations damper (TOD) by inducing a term proportional to the generator's speed change in the generator's electro-magnetic torque. Manoeuvres like assigning a constant [8, 11, 12] or smooth reference for active power/torque controller [6], implementing MPPT schemes based on tip speed ratio control [13, 14], and operating in above nominal wind speeds significantly deteriorate the natural damping effect provided by the optimum power curve-based MPPT process. An effective solution is to design a supplementary control loop for active damping resolutions. In this context, the band-pass (BP) filtered data of the generator's speed is used and proper phase compensation is discussed to modulate the permanent magnet synchronous generator (PMSG)'s power/torque reference and induce a desired electrical damping torque [6, 15, 16]. However, this method is highly dependent on drive-train parameters that are subject to uncertainties. In this regard, proposals exist to utilize unfiltered data of the generator's speed and feedforward controllers for the specification of proper stabilizing torque reference [17, 18]; however, torsional oscillations will still be injected into the DC link and then into the power system. Model reference-based approaches have also been considered for state estimation and designing robust active TODs. However, those approaches require accurate wind speed estimation, which is challenging [19, 20]. Advanced active TODs have been proposed in [13, 14] to merely increase the damping of the free-free torsional oscillations through processing both generator and turbine speeds. The literature [7, 21] has discussed and shared different approaches to independently compensate for poor characteristics of type-4 WTG's stiffness and damping. However, the implementation approaches proposed by [7, 21] cannot be applied to the second structure of DC voltage control due to the disturbance rejection phenomenon of the fast DC voltage controllers. In more detail, adding feedforward elements to the output of the DC voltage controller to modulate reference torque/power will be ineffective because it would cause variations in the DC voltage. Consequently, the fast DC voltage controller will effectively cancel the feedforward elements from the torque/power reference as a part of the disturbance rejection phenomenon to stabilize DC voltage [10, 22]. Passive TODs are usually avoided to avoid increasing the system's losses and maintenance requirements due to adding extra mechanical components [23].

In the first structure of DC voltage control, small-signal dynamics of two sides of the WTG's DC link are decoupled if WTG does not participate in frequency control by providing its kinetic energy [24]. Therefore, torsional oscillations can be stabilized at the MSC without taking the GSC 's dynamics into account, and the dynamics of turbine and MSC can be neglected in analyzing power system stability. Such DC decoupling is absent in the frequency responsive WTGs due to high coupling between the drive-train and power system frequency [25]. Thus, new active TODs should be designed at the power system level and entire WTG dynamics should be modeled to investigate power system stability.

For the second DC voltage control structure, which has better low voltage ride-through performance, there are fewer deep research studies on designing active TODs. In this control structure, the MPPT is performed by the active power control unit of the GSC that cannot provide inherent damping to torsional oscillations regardless of the employed MPPT strategy. In other words, no term proportional to the generator's speed change would be induced in the generator's electro-magnetic torque [6]. In this control structure, damping torque can be induced by modulating the reference of the DC link's voltage or the GSC's power using BP-filtered data of the generator's speed and proper phase compensations [6]. Modulation of the DC link's voltage will minimize the injection of torsional oscillations into the power system; however, it has a limited performance due to its sensitivity to the drive-train's parameter uncertainty and the low permissible range for variations of the DC-link voltage to prevent overmodulation of the converters and impermissible blocking voltage of the semiconductors [10, 22]. In more detail, accurate identification of the natural frequency of the torsional oscillations is needed, which is challenging because of the drive-train's parameter uncertainty. Also, the interaction of the WTG and power system might change the frequency of the torsional oscillations to a certain extent. In this sense, it is recommended to employ an unfiltered speed of the generator and design feed-forward control loops to contribute to the specification of the generator's torque reference [10]. However, the high bandwidth of the DC voltage controller will lead to a disturbance rejection effect and attenuate the intended active damping. Thus, the bandwidth of the DC voltage controller has been reduced in [10, 22] which would have a detrimental effect on the stability of the DC voltage when an AC fault occurs or wind speed changes. Furthermore, modulation of GSC's active power reference is ineffective if the VSG concept is adopted to control the GSC. It is since VSG's active power

controller has low bandwidth to provide inertia effectively [26].

Another issue in the second DC voltage control structure is the absence of decoupling between small-signal dynamics of two sides of the DC-link's capacitor. This issue would be maximized if the virtual inertia emulation concepts (like the VSG) are implemented to make the WTGs frequency responsive by providing the stored kinetic energy to the grid as significant coupling will exist between the masses of the WTG and grid's generators [26–28, 4, 1]. Note that the second control structure is more suitable for realizing the concept of frequency-responsive WTGs. It is because the GSC cannot ensure high bandwidth for closed-loop DC voltage control due to the low bandwidth of the employed VSG's active power controller. Therefore, the entire dynamics of WTG and power system should be taken into account when designing active TODs, because changes in power system structure and dynamics might deteriorate the performance of traditional BPF filter-based active TODs.

Nevertheless, impacts of torsional dynamics of drive-train on the frequency control schemes and power system dynamics have been paid less attention over previously published research works on VSG-regulated type-4 WTGs and also other frequencies responsive WTGs (research gap). In those research works, drive-train dynamics have been modelled by a single mass [1, 3, 4, 25, 28].

## 1.3 | Contributions

The contributions of this research work are threefold:

- The small-signal (frequency) stability analysis of a complete power system is extended by considering drive train oscillations of VSG-regulated type-4 WTGs. An unstable torsional oscillatory mode is found and analyzed and the mechanism of the instability is identified.

A comprehensive modal analysis and characterization are carried out using participation factor analysis (PFA). The aim is to characterize the eigenvalues of the power system when multi-mass-spring models are used for the WTG's drive-train. Impacts of the VSG's key control parameters on the system's eigenvalues are analyzed and stability margins are identified. An unstable eigenvalue is found that is related to drive train (torsional) oscillation and would further destabilize if the emulated virtual inertia constant ($H_v$) decreases. Instability originates from a lack of inherent damping provided by the WTG itself and its controllers. The instability mechanism is clearly described using the results of PFA, which reveals that because of the adoption of the VSG controller, the dynamics of the drive train shaft, emulated virtual swing equation, and the external network (and its feedback mechanisms) interact with each other. In more detail, the VSG enforces the MPPT by processing the generator's speed. Simultaneously, it synchronizes the GSC of the WTG to the rest of the power system; therefore, its couples the dynamics of WTG and the rest of the power system. A decrease of $H_v$ would increase the bandwidth of VSG's active power controller (APC) and the discussed coupling; therefore, it would further intensify the instability mechanism by profounding the injection of the unstable power oscillations into the grid

- A comprehensive active TOD (CA-TOD) is presented that can adjust/increase both the frequency and damping ratio of torsional oscillations independently.

To ensure robust drive train stability concerning variations of $H_v$ and uncertainties of drive train parameters, a comprehensive active TOD (CA-TOD) is presented that, unlike previous methods [13, 14], is capable of adjusting both the frequency and damping ratio of torsional oscillations independently. It is done through proper processing of the turbine-generator set's speed difference. By sufficiently increasing the torsional oscillations frequency (out of bandwidth of VSG's APC) and damping ratio, those oscillations will be damped and contained in the WTG level, will be almost decoupled from dynamics of the VSG and external network, and will not penetrate the power system; therefore, CA-TOD can be tuned locally at the WTG level.

- A method is proposed to implement the CA-TOD by hosting a supercapacitor unit to the WTG's DC link and designing and tuning properly coordinated controllers. Also, a state of charge (SoC) controller is proposed and tuned to recover the supercapacitor's voltage without deteriorating the performance of CA-TOD and impairing power system dynamics.

To realize the CA-TOD, a supercapacitor unit is hosted to the WTG's DC link and associated controllers are designed considering the system's physical and control constraints. Coordinated controllers are proposed for the supercapacitor and MSC to effectively circulate the proposed stabilizing power between the ESS, DC link, and permanent magnet generator while not inducting variations in the DC link's voltage. A state of charge (SoC) controller is proposed that determines the reference speed difference for the turbine-generator set. A tuning method is proposed for related control parameters to recover the supercapacitor's charge/voltage without deteriorating the performance of CA-TOD or imposing significant impacts on the power system dynamics.

The effective/robust functioning of the CA-TOD is evaluated and its superior performance to the BP filter and phase compensation-based active TOD is demonstrated. In this context, a sensitivity analysis is conducted by varying the key control parameters of the VSG and examining the impacts of uncertainties in the drive-train's parameters. Both small-signal analysis and electro-magnetic transient (EMT) simulations are performed in MATLAB/Simulink platform regarding an aggregated wind farm connected to a single machine power system. The key findings are also cross-verified by performing EMT simulations on a detailed 75 MW wind farm connected to a multimachine power system.

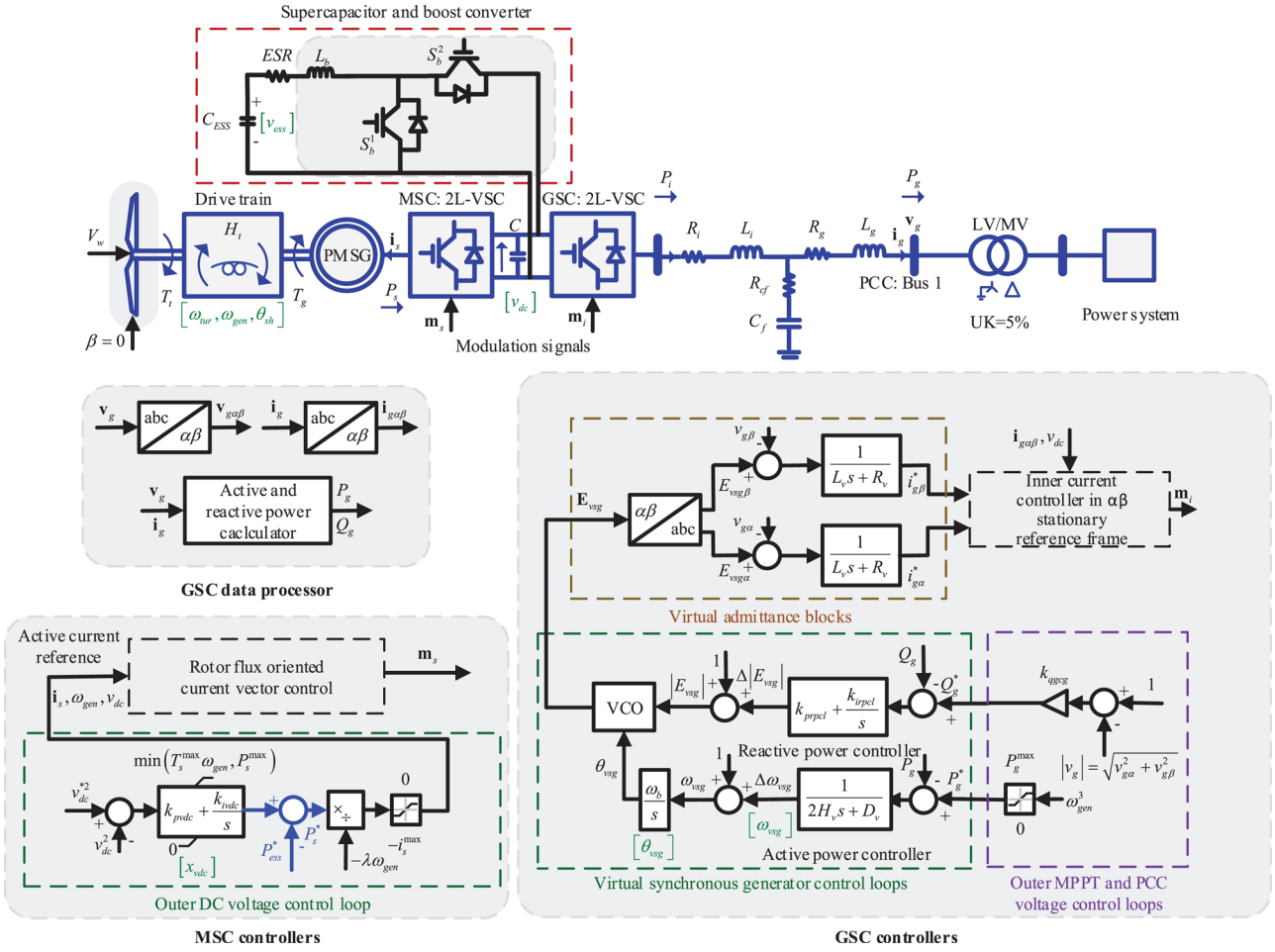


**FIGURE 1** Physical and control structure of the VSG-regulated type-4 WTG and introduced ESS unit

## 2 | MODELLING AND CONTROL OF THE POWER SYSTEM UNDER STUDY

This part describes the model and control structure of the type-4 WTG system that is connected to a balanced, relatively strong (with high short circuit current capacity), and two-machine power system. The system's fundamental frequency and electromechanical timescale model is outlined and linearized to study power system frequency stability. This paper uses a per-unit system to represent all variables, parameters, and formulas; however, time and angle are still in seconds and radians.

### 2.1 | Modelling of the VSG-regulated type-4 WTG system

The physical and control structure of a 5 MW, direct-drive, and VSG-regulated type-4 WTG is provided in Figure 1 [26]. The system includes 3-p blades connected to the rotor, drive-train, PMSG, MSC, DC link, GSC, LCL filter [24], and LV/MV (3 kV/33 kV) transformer units. The fast-switching dynamics of the (three-phase, two-level, and six-switch) MSC and GSC are neglected in EMT and small-signal studies by adopting averaged models. The full model of the WTG is considered for EMT studies [24]; however, very fast electrical dynamics related to the PMSG's stator [12], LCL filter, LV/MV transformer, and inner current control loops of the MSC and GSC are neglected in small-signal studies. The rest of the WTG is modelled in the following subsections.

#### 2.1.1 | Aerodynamic wind energy conversion

The captured aerodynamic power ($P_t$) and torque ($T_t$) by the 3-p blades can be calculated by (1)–(3).

$$P_t = C_p(\lambda,\beta)\, V_w^3 / C_p^{\max},\quad T_t = P_t/\omega_{tur} \tag{1}$$

$$C_p(\lambda,\beta) = \left(c_1 c_2 \frac{1}{\Lambda} - c_1 c_3 \beta - c_1 c_4 \beta^{c_5} - c_1 c_6\right) e^{-c_7/\Lambda} \tag{2}$$

$$\frac{1}{\Lambda} = \frac{1}{\lambda\lambda^{\max} + c_8\beta} - \frac{c_9}{1+\beta^3},\quad \lambda = \frac{\omega_t}{V_w} \tag{3}$$

where $V_w$ and $\beta$ variables represent wind speed and pitch angle respectively [26]. Also, $[c_1 \ldots c_9]$, $C_p^{max}$, and $\lambda^{max}$ are the WTG's

characteristic parameters. WTG's power performance coefficient is symbolized by $C_p(\lambda,\beta)$ that is a function of tip speed ratio ($\lambda$) and $\beta$. $C_p(\lambda,\beta)$ would be equal to $C_p^{max}$ if the WTG operates within the MPPT region (4 m/s < $V_w$ < 11.68 m/s).

Presented equations for the $T_t$ can be linearized at $[\omega_{tur0}, \beta_0, V_{w0}]$ equilibrium as (4)-(8) to model the incremental change of $T_t$ ($\Delta T_t$) in response to $\Delta V_w$, $\Delta\beta$, and $\Delta\omega_{tur}$. Symbol $\Delta$ and subscript 0 represent incremental value and steady-state value of their related variables.

$$\Delta T_t = (1/\omega_{tur0})(\Delta P_t) - \left(P_{t0}/\omega_{tur0}^2\right)(\Delta\omega_{tur}) \tag{4}$$

$$\Delta P_t = \left.\frac{\partial P_t}{\partial V_w}\right|_{\left[V_{w0}\ \beta_0\ \omega_{tur0}\right]}(\Delta V_w) + \left.\frac{\partial P_t}{\partial \beta}\right|_{\left[V_{w0}\ \beta_0\ \omega_{tur0}\right]}(\Delta\beta) + \left.\frac{\partial P_t}{\partial \omega_{tur}}\right|_{\left[V_{w0}\ \beta_0\ \omega_{tur0}\right]}(\Delta\omega_{tur}) \tag{5}$$

$$\left.\frac{\partial P_t}{\partial V_w}\right|_{\left[V_{w0}\ \beta_0\ \omega_{tur0}\right]} = \frac{3V_{w0}^2 C_p(\lambda_0,\beta_0)}{C_p^{\max}} - \frac{V_{w0}\omega_{tur0}}{C_p^{\max}}\left.\frac{\partial C_p(\lambda,\beta)}{\partial\lambda}\right|_{\left[V_{w0}\ \beta_0\ \omega_{tur0}\right]} \tag{6}$$

$$\left.\frac{\partial P_t}{\partial \beta}\right|_{\left[V_{w0}\ \beta_0\ \omega_{tur0}\right]} = \frac{V_{w0}^3}{C_p^{\max}}\left.\frac{\partial C_p(\lambda,\beta)}{\partial\beta}\right|_{\left[V_{w0}\ \beta_0\ \omega_{tur0}\right]} \tag{7}$$

$$\left.\frac{\partial P_t}{\partial \omega_{tur}}\right|_{\left[V_{w0}\ \beta_0\ \omega_{tur0}\right]} = \frac{V_{w0}^2}{C_p^{\max}}\left.\frac{\partial C_p(\lambda,\beta)}{\partial\lambda}\right|_{\left[V_{w0}\ \beta_0\ \omega_{tur0}\right]} \tag{8}$$

### 2.1.2 | Drive-train

The two-mass model models the dynamics of the (lossless) drive-train in (9)–(11) to study torsional oscillations (11). This model receives driving torques $T_t$ and $T_s$ (PMSG's electrical torque) as inputs.

$$\frac{d\omega_{tur}}{dt} = \frac{D_{tg}}{2H_t}\left(\omega_{gen}-\omega_{tur}\right) - \frac{K_{sh}}{2H_t}\theta_{sh} + \frac{1}{2H_t}T_t \tag{9}$$

$$\frac{d\omega_{gen}}{dt} = \frac{D_{tg}}{2H_g}\left(\omega_{tur}-\omega_{gen}\right) + \frac{K_{sh}}{2H_g}\theta_{sh} - \frac{1}{2H_g}T_s \tag{10}$$

$$\frac{d\theta_{sh}}{dt} = \omega_{MelB}\left(\omega_{tur}-\omega_{gen}\right) \tag{11}$$

In (9)–(11), $H_t$, $H_g$, $K_{sh}$, $D_{tg}$, and $\omega_{MelB}$ are parameters that represent the turbine's inertia constant (in seconds [s]), generator's inertia constant (in seconds [s]), shaft's stiffness (in per unit/electrical rad), shaft's damping coefficient (in per unit), and base rotational speed respectively. Also, $\omega_{tur}$, $\theta_{tur}$, $\omega_{gen}$, $\theta_{gen}$, and $\theta_{sh}$ are the variables that characterize the turbine's rotational speed (in per unit), turbine's angle (in radian [rad]), generator's rotational speed (in per unit), generator's angle (in radian [rad]), and shaft's torsional angle (in radian, [rad]) respectively. The torsional torque of the shaft ($T_{sh}$) is defined as, $T_{sh} = K_{sh}\,\theta_{sh} + D_{tg}(\omega_{tur}-\omega_{gen})$.

### 2.1.3 | PMSG

PMSG's electro-magnetic torque $T_s$ is represented and linearized as a function of the generated air gap power ($P_s$) and $\omega_{gen}$ by algebraic equations reported in (12). Due to the lossless drive train and neglecting of stator losses $P_{s0}$ is equal to $P_{t0}$.

$$T_s = P_s/\omega_{gen};\ \Delta T_s = \left(1/\omega_{gen0}\right)(\Delta P_s) - \left(P_{s0}/\omega_{gen0}^2\right)(\Delta\omega_{gen}) \tag{12}$$

### 2.1.4 | Power converters and DC link's capacitor

The voltage dynamic of the DC-link's capacitor ($v_{dc}$) is modelled by the differential equation of (13) considering the ($P_s$–$P_i$) power difference where $P_i$ represents the instantaneous power absorbed by the GSC and will be calculated in the next subsections.

$$\frac{C}{\omega_{MelB}}\frac{dv_{dc}^2}{dt} = P_s - P_i \tag{13}$$

### 2.1.5 | LCL filter and LV/MV transformer

The phasor modelling approach is employed and the LCL filter is substituted by the virtual impedance ($X_v$) emulated by the VSG unit. Such substitution is justified because of the very high bandwidth of the GSC's current controller (around 500 Hz) that ensures effective virtual impedance emulation in the electromechanical time scale, refer to Section 2.2.2. Similarly, LV/MV transformer is modelled by its series/leakage impedance in the fundamental frequency.

## 2.2 | Control of the VSG-regulated Type-4 in the MPPT region

Regarding high-level control objectives, the MSC regulates the DC link voltage and reactive current generated by the PMSG; while the GSC is in charge of MPPT and grid voltage regulation. This research focuses on the (upper middle) MPPT region and small disturbances which imply that the $\omega_{tur}$ and $P_s$ would be below their rated values over the entire transient regime; Therefore, the pitch angle control unit would remain inactive ($\beta = 0$) and it is possible to exclude its dynamics from the modelling.

### 2.2.1 | Machine side converter

The MSC employs a rotor field-oriented (RFO) scheme for decoupled control of PMSG's current vector ($\boldsymbol{i_s}$) and specification of the modulation references ($\mathbf{m}_s$) [24] [29]. Also, $T_s$ is modelled by $T_s = -\lambda_s i_{sq}$ where $\lambda_s$ is the stator flux linkage established by permanent magnets and $i_{sq}$ is the active current component. The reference values of variables are symbolled by * superscripts.

The MSC regulates the DC voltage square ($v_{dc}^2$) by the specification of appropriate $P_s^*$ as [14], $\Delta v_{dc}^{*2} = 0$. The $P_s^* = P_s$ equality holds for small signal studies because $P_s^*$ is regulated through the direct specification of $i_{sq}^*$ in Figure 1 in an open-loop mechanism and ideal tracking of $i_{sq}^*$ is assumed for the employed RFO current vector controller.

$$P_s^* = \left(k_{pvdc} + \frac{k_{ivdc}}{s}\right)\left(v_{dc}^{*2} - v_{dc}^2\right) \tag{14}$$

The related DC voltage controller is designed by considering the dynamic equation of (13) system and assuming $P_i$ as an external disturbance. The aim was to reach bandwidth and phase margin of 50 Hz and 80°, respectively ( $k_{pvdc} = 10.39$ and $k_{ivdc} = 575.85$) following the design approach of [30]. Accordingly, $i_{sq}^*$ is generated for the PMSG by $i_{sq}^* = P_s^* / (-\lambda_s \omega_{gen})$ relation.

### 2.2.2 | Grid side converter

*Inner current control loops*

Nonideal proportional resonance (PR) controllers are adopted to realize the current controllers of the GSC in the $\alpha\beta$ stationary reference frame and to specify the modulation signals for the GSC ($\mathbf{m}_i$) [5], [24]. Parameters of the PR controllers are designed by applying the design guidelines of [31] to reach the bandwidth of 500 Hz for current reference tracking.

*Virtual synchronous generator*

The GSC employs the VSG as the core controller to emulate simplified electromechanical (e.g. inertial frequency response) and electrical characteristics of a synchronous generator (SG) [32]. From Figure 1, the VSG includes an active power controller (APC) that processes the reference tracking error of the GSC's active power ($P_g^* - P_g$) measured at PCC bus and characterizes the frequency response o)f the GSC. In the APC, the swing equation of (15), which includes characteristic parameters of $H_v$ (inertia constant) and $D_v$ (damping coefficient), is implemented as the controller to specify the incremental virtual synchronous frequency ($\Delta\omega_{vsg}$). Base grid frequency is added to $\Delta\omega_{vsg}$ as a feedforward term to obtain $\omega_{vsg}$. Angle ($\theta_{vsg}$) of virtual electro-motive force (EMF ($E_{vsg}$) is determined by integrating the $\omega_{vsg}$. A suitable phase difference between $E_{vsg}$ and $v_g$ (voltage of PCC bus in Figure 1), ensures natural grid synchronization and active power regulation of the GSC.

$$\Delta P_g^* - \Delta P_g = 2H_v \frac{d\Delta\omega_{vsg}}{dt} + D_v \omega_{vsg} \tag{15}$$

Meanwhile, a reactive power controller (RPC) regulates the GSC's reactive power ($Q_g$) measured at the PCC bus to its reference $Q_g^*$ by a PI controller and calculates the incremental voltage magnitude of virtual EMF ($\Delta E_{vsg}$).

$$\Delta\left|E_{vsg}\right| = \left(k_{prpcl} + \frac{k_{irpcl}}{s}\right)\left(Q_g^* - Q_g\right) \tag{16}$$

$E_{vsg}$ is then calculated by adding base virtual EMF voltage to the $\Delta E_{vsg}$ using a feedforward term. Three-phase EMF voltages ($\mathbf{E_{vsg}}$) are generated by the voltage-controlled oscillator (VCO) unit ($E_{vsga} = E_{vsg}\cos(\theta_{vsg})$, $E_{vsgb} = E_{vsg}\cos(\theta_{vsg}-2\pi/3)$, and $E_{vsge} = E_{vsg}\cos(\theta_{vsg}+2\pi/3)$) and transformed to $\alpha\beta$ stationary reference frame and symbolized by $\alpha$ and $\beta$ subscripts.

A virtual admittance in the form of $1/(R_v+jX_v)$ is also emulated on two ends of the LCL-R filter ( $L_v = X_v/2\pi$) through the specification of proper current references in the $\alpha\beta$ stationary reference frame ($i_{g\alpha}^*$ and $i_{g\beta}^*$). Thanks to the high bandwidth of the inner current control loops, virtual admittance would be effectively emulated and its time constant would characterize the electrical characteristic of the VSG/GSC. With proper values for $R_v$ and $jX_v$ external grid can be made inductive. Assuming a high $X_v/R_v$ ratio and a low load angle ($\angle E_{vsg} - \angle v_g$), decoupled control of $P_g$ and $Q_g$ can be realized by regulation of the $\theta_{vsgs}$ and $|E_{vsg}|$ respectively.

Parameters of the VSG's APC are designed to emulate a typical synchronous generator with characteristic parameters of $H_v = 5$, $D_v = 1$, $X_v = 0.2$, and attenuate electrical resonances ( $R_v = 0.05$). Finally, the PI controller of the reactive power regulator is tuned following the design approach of [26] to attain the closed-loop bandwidth (CBW) of 20 Hz for $Q_g(s)/Q_g^*(s)$ ($k_{prpcl} = 0$ and $k_{irpcl} = CBW \times X_v$) [26].

*Outer control loops*

According to Figure 1, $P_g^*$ is specified by the adopted MPPT process as [17] while considering the maximum power capacity of the GSC ($P_g^{max}$). $\Delta P_g^*$ is also presented in [17] to develop the final small-signal model. Also, $Q_g^*$ is determined by a reactive power ($Q_g^*$) -voltage ($|v_g|$) droop controller respectively. Therefore, the WTG would follow an optimized and prespecified $P_g - \omega_{gen}$ curve and can provide voltage support to weak and islanded grids. Due to the assumed strong grid property, dynamics of the outer $Q_g^* - |v_g|$ loop and VSG's RPC are neglected in the modal analysis.

$$P_g^* = \omega_{gen}^3;\ \Delta P_g^* = 3\omega_{gen0}^2 \Delta\omega_{gen} \tag{17}$$

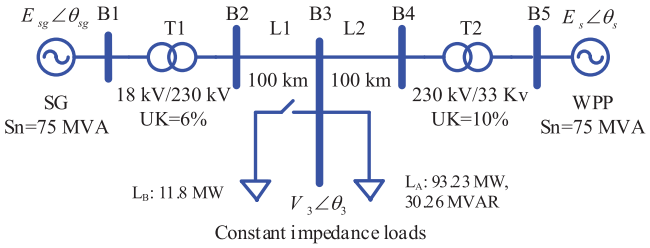


**FIGURE 2** Generic two-machine test power system inclusive of an aggregated 75 MW wind power plant

## 2.3 | Two machine power system

A generic two-machine and five-bus network, see Figure 2, is studied to investigate the impacts of drive-train dynamics of VSG-regulated type-4 WTGs on the power system stability, to evaluate effective permanence and impacts of the TODs, and to identify the stability limits. In this system, $G_1$ represents a 75 MW steam turbine power plant and $G_2$ represents an aggregated 75 (15×5) MW wind power plant. In the EMT model, $G_1$ is equipped with a reheater, governor, synchronous generator (represented by the seventh order model), and static excitation system [33]. Typical per unit parameters reported in [34] are assumed for the synchronous generator and transmission lines.

For the small modelling purpose, a suitable model of the $G_1$ turbine that is reported in [35] and shown in Figure 3 is taken where some nonlinearities and faster dynamics are avoided because the time constant of the reheater would effectively characterize the essential dynamics of the steam turbine power plant. The power system responds to wind speed ($\Delta V_w$) and load variations ($\Delta P_L$). The synchronous generator is modelled by the second-order model and the action of the excitation system is neglected due to the assumed strong grid property. Finally, to derive active power injection of the VSG and $G_1$ units ($P_g \cong P_i$ and $P_{sg}$) as functions of their back EMF angles ($\theta_{vsg}$ and $\theta_{sg}$) and $\Delta P_L$, the network's impedances are properly added to the virtual impedance of the VSG unit and transient impedance of the synchronous generator, the system's power flow equations are derived; and Kron's reductions are properly enforced [34]. $K_{sg\text{-}vsg} = 1.1822$, $K_{L1} = 0.4322$, and $K_{L2} = 0.5678$ in [18], and the rest of the network's parameters are reported in the appendix.

$$\begin{bmatrix}\Delta P_g\\ \Delta P_{sg}\end{bmatrix} = \begin{bmatrix}K_{sg-vsg} & -K_{sg-vsg}\\ -K_{sg-vsg} & K_{sg-vsg}\end{bmatrix}\begin{bmatrix}\Delta\theta_{vsg}\\ \Delta\theta_{sg}\end{bmatrix} + \begin{bmatrix}K_{L1}\\ K_{L2}\end{bmatrix}\Delta P_L \tag{18}$$

## 2.4 | Methodology for small signal studies

Based on the presented derivations and discussions, linearized dynamics of the test two machine power system are developed in Figure 3 by developing and interconnecting linearized models of the involved subsystems and neglecting protection controllers. The initial operating point for the linearization of the equations is identified considering the initial wind speed and conducting power flow analysis. A common per unit system is considered in developing the linearized model of Figure 3 by assuming base power and base voltage to be 75 MW and 230 kV respectively. In this model, $\Delta V_w$ and $\Delta P_L$ are the input disturbance and dynamics of the CA-TOD, integrated supercapacitor, and proposed SoC controller can be included in the modelling which will be discussed in Section 4. From Figure 3, the wind and thermal power plants are parts of closed-loop feedbacks that might destabilize the oscillations of the WTG's drive-train and power system's frequency. In other words, the stability of VSG-regulated type-4 WTGs and the performance of the related TODs should be analyzed in the context of broader power system stability.

The presented dynamic model is implemented in the MATLAB/Simulink platform, and the power system's eigenvalues ($\lambda_i = \sigma_i \pm j\omega_i$) and left ($\psi_i$) and right ($\phi_i$) eigenvectors are obtained using the *eig* command of the software [33]. The damping ratio ($\xi_i$) and damped frequency ($f_i$) of an eigenvalue are then calculated. Finally, normalized participation factors are obtained to evaluate the level of participation of the state variable ($x_k$) in the formation of the eigenvalue ($\lambda_i$) [33].

# 3 | UNCOMPENSATED WTG SYSTEM CONNECTED TO THE TWO MACHINE POWER SYSTEM: MODAL ANALYSIS

In this part, the small-signal stability of the integrated two-machine power system is analyzed with a particular focus on the impacts of torsional oscillations on frequency stability. No active/passive TOD is implemented on the WTG system. The root cause of the destabilizing impacts of the drive-train on the system's frequency is identified and the influences of VSG's key control parameters on the stability of the system's eigenvalues are studied.

## 3.1 | Free-free torsional oscillations

To conduct a preliminary analysis of (free–free) torsional oscillations, the dynamics of $\theta_{sb}$ can be obtained as [19] from (9)–(11).

$$\frac{d^2\theta_{sb}}{dt} + D_{tg}\left(\frac{1}{2H_t}+\frac{1}{2H_g}\right)\frac{d\theta_{sb}}{dt} + \omega_{MelB}K_{sb}\left(\frac{1}{2H_t}+\frac{1}{2H_g}\right)\theta_{sb} = \frac{\omega_{MelB}T_t}{2H_t} - \frac{\omega_{MelB}T_e}{2H_g} \tag{19}$$

Having a second-order differential equation in (19); the transient behaviour of the free-free system can be explained by natural frequency ($\omega_n^{sb}$) and damping ratio ($\xi_n^{sb}$) of the oscillations:

$$\omega_n^{sb} = \sqrt{\frac{\omega_{MelB}K_{sb}}{2}\frac{H_t+H_g}{H_tH_g}} \tag{20}$$

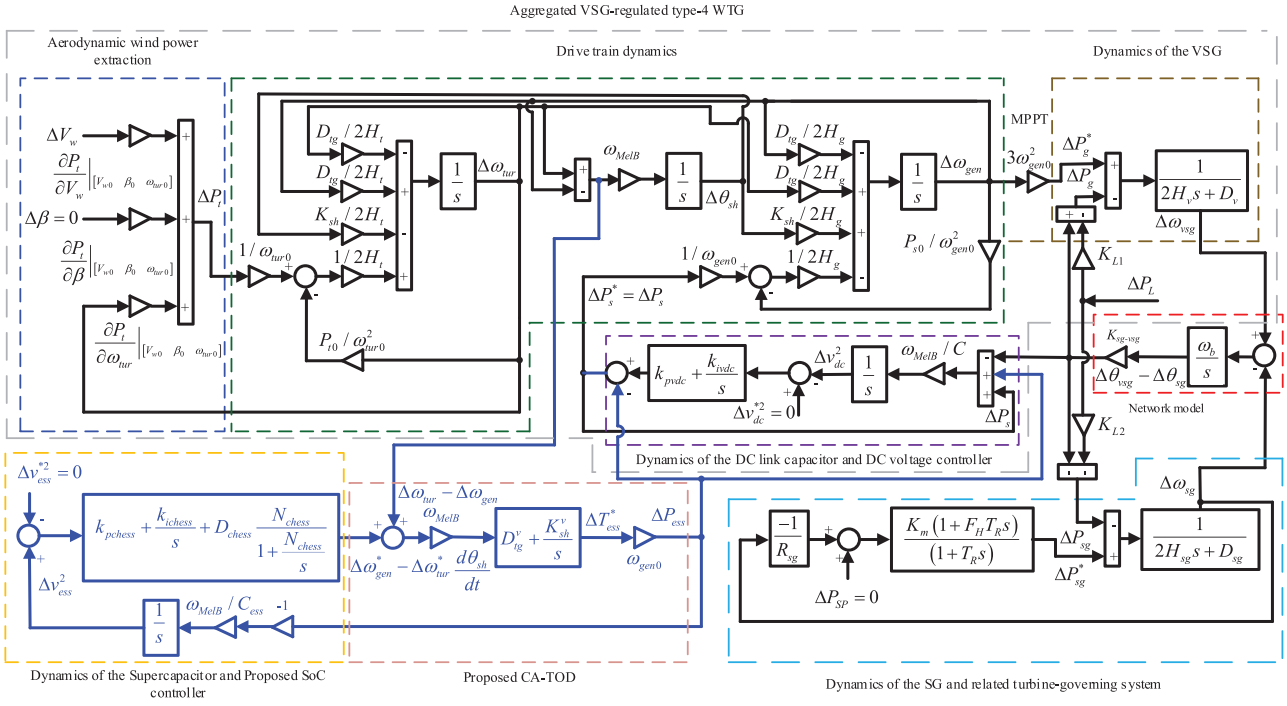


**FIGURE 3** Representation of the simplified linearized dynamics of the test two machine power system by block diagrams

**TABLE 1** Characteristics of eigenvalues of the test two machine power system comprised of uncompensated VSG-regulated type-4 WTG

| Eigenvalue | Frequency (HZ) | Damping ratio (%) | State variables with the highest participation factor |
|---|---|---|---|
| LF1 | 0 | 100 | $v_{dc}(1), x_{vdc}(0.3)$ |
| LF2 | 0 | 100 | $x_{vdc}(1), v_{dc}(0.3)$ |
| LF3 | 1.36 | 4.49 | $\theta_{vag-sg}(1), \omega_{sg}(0.5), \omega_{vsg}(0.49), \theta_{sh}(0.10), \omega_{tur}(0.03), \omega_{gen}(0.01)$ |
| LF4 | 0 | 100 | $\omega_{tur}(1), x_{gov}(0.27), \omega_{vsg}(0.16), \omega_{gen}(0.13), \omega_{sg}(0.01)$ |
| LF5 | 0.05 | 47.40 | $x_{gov}(1), \omega_{vsg}(0.68), \omega_{sg}(0.6), \omega_{tur}(0.41), \omega_{gen}(0.05)$ |
| **LF6** | **2.27** | **−4.16** | $\theta_{sh}(1), \omega_{gen}(0.88), \omega_{tur}(0.11), \theta_{vag-sg}(0.06), \omega_{vsg}(0.05), \omega_{sg}(0.01)$ |

$$\xi_{sh} = \frac{D_{tg}}{4\omega_n^{sh}} \frac{H_t + H_g}{H_t H_g} = \frac{D_{tg}}{2} \sqrt{\frac{1}{2\omega_{MelB} K_{sh}} \frac{H_t + H_g}{H_t H_g}} \tag{21}$$

Substituting the system's parameters from the [appendix], $\omega_n^{sh} = (2 \times \pi) \times 2.27\ Hz$ and $\xi_n^{sh} = 0.0017$ that indicates marginal stability of the torsional oscillations.

## 3.2 | Modal analysis

In this part, the characteristics of the eigenvalues of the integrated test system are described. The wind speed is set to be 10.68 m/s which is within the MPPT region of the considered WTG.

According to the modal analysis results, the system has nine eigenvalues, see Figure 4. The results of PFA for these eigenvalues are reported in Table 1 where only participation factors for key involved state variables are reported. From Table 1, the damping ratios of LF modes (except LF3 and LF6) are high; however, there exists unstable (LF6) and a poorly damped eigenvalue (LF3).

Table 1 shows that LF1 and LF2 eigenvalues are related to the dynamic interaction of the DC link's capacitor and its voltage controller and represent the DC voltage regulation process the specification of $P_s^*$. LF1 and LF2 eigenvalues have damping ratio of 100% and will be damped quickly as they are located far from the left side of the $j\omega$ axis, see Figure 4.

According to PFA, the poorly damped LF3 eigenvalue with the damped frequency of 1.36 Hz represents the inter-area oscillations between the thermal and wind power plants. Participation of $\theta_{sh}$, $\omega_{tur}$, and $\omega_{gen}$ in the formation of LF3 eigenvalue indicates that drive-train dynamics are reflected on the inter-area oscillations and demonstrates effective coupling of the power system and drive-train dynamics.

The LF4 eigenvalue is mainly linked to the dynamic interaction of $\omega_{tur}$, $x_{gov}$, $\omega_{vsg}$, $\omega_{gen}$, and $\omega_{sg}$ state variables and originates from the MPPT process. In more detail, the APC

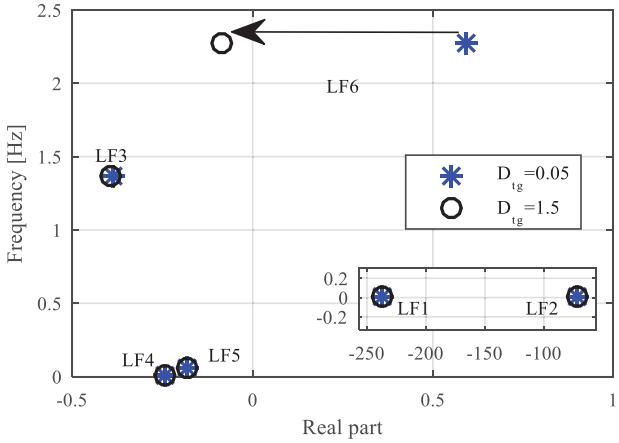


**FIGURE 4** Eigenvalues of the test two machine power system comprised of uncompensated VSG-regulated type-4 WTG

of the VSG regulates the turbine/generator speed according to the implemented MPPT philosophy by exchanging power with the power system that in turn impacts the system frequency and actuates the thermal power plant's governor to regulate the system frequency. The very low frequency and well-damped LF5 eigenvalue is formed due to the dynamic interaction of $x_{gov}$, $\omega_{vsg}$, $\omega_{sg}$, $\omega_{tur}$, and $\omega_{gen}$ state variables and show the process of system frequency regulation by the thermal power plant's governor through its droop controller.

Lastly, the unstable LF6 eigenvalue represents the WTG's torsional oscillations because the PFA shows the participation of $\theta_{sh}$, $\omega_{gen}$, $\omega_{tur}$, $\theta_{vsg-sg}$, $\omega_{vsg}$ and $\omega_{sg}$ state variables. Since the frequency of torsional oscillations (2.27 Hz) is close to the bandwidth of the VSG's APC ($BW_{VSG\text{-}APC}$), the $\omega_{vsg}$ and accordingly $\theta_{vsg-sg}$ and $\omega_{sg}$ state variables gained participation in the formation of the LF6 eigenvalue. In consequence, unstable oscillations would be injected into the power system; would destabilize it through active power injection of the WTG; would appear in the $\theta_{vsg-sg}$ (and hence inter-area power) and system frequency ($\omega_{vsg}$ and $\omega_{sg}$). Also, this unstable oscillation will appear in the $\theta_{sh}$, $\omega_{gen}$, $\omega_{tur}$, and other electrical variables of the WTG. The damped frequency and damping ratio of LF6 eigenvalue are 2.27 Hz and −4.16% respectively which indicates an unstable condition. The natural frequency of torsional oscillations ($2.27\ \text{Hz}/\sqrt{1-0.0416^2}$) is close to what was calculated by [20]; however, the difference in the damping ratio of LF6 and prediction of [21] is due to the impacts of the VSG's APC and overall power system dynamics. Stabilization of the torsional oscillations is the main goal of this paper. The identified unstable interaction of the drive train dynamics and power system frequency was not found in the recent studies on the VSG-regulated WTGs because drive-train dynamics have been modelled by a single mass model [1, 3, 4, 25, 28].

From the PFA of the LF3-LF6, it is found that there is a coupling between the state variables existing at two sides of the DC link's capacitor. For instance, $\theta_{vsg-sg}$, $\omega_{vsg}$, and $\omega_{sg}$ participate in the formation of the torsional oscillations eigenvalue (LF6). This is unlike the first structure of DC voltage control for type-4 WTGs where state variables that exist on one side of the DC link's capacitor will not participate in the formation of eigenvalues related to the other side [24].

### 3.2.1 | Sensitivity analysis: Variation of $D_{tg}$

The modal analysis is done once more by increasing the $D_{tg}$ from 0.05 to 1.5; however, such a large value for $D_{tg}$ is unrealistic as the WTG system has no inherent damping. Due to the increased value of the $D_{tg}$, the LF6 eigenvalue is stabilized by moving to the left side of the $j\omega$ axis, see Figure 4. This is in turn in line with calculations of [21]. Moreover, the increase in the value of the $D_{tg}$ has no impact on other WTG's eigenvalues. Therefore, it is possible to mention that the absence of inherent damping is the main reason for the instability of the LF6 eigenvalue.

### 3.2.2 | Sensitivity analysis: Variation of VSG's key parameters ($H_v$ and $D_v$)

The modal analysis is done again to study the impacts of variations of VSG's key parameters (within the reasonable range) on the power system's eigenvalues.

From Figure 5a, $H_v$ increase leads to migration of the unstable LF6 eigenvalue toward the left side of the $j\omega$ axis and stabilizes the torsional oscillations without changing the related damped frequency. This is because the bandwidth of VSG's APC reduces by the $H_v$ increase; therefore, the flow of oscillatory terms presents in the $P_g^* = \omega_{gen}^3$ into the power system would be reduced. In more detail, the filter effect that the virtual mass exerts by attenuating the reflection of the oscillatory terms of the $P_g^*$ on $\omega_{vsg}$ becomes more profound by the $H_v$ increase. Accordingly, detrimental dynamic interaction between the drive-train and the rest of the integrated system is attenuated. Stabilizing torsional oscillations by $H_v$ increase is not preferred; because the proper value of $H_v$ should be identified after satisfying some (even conflictory) requirements of the power system (e.g. decreasing rate of change of frequency (RoCoF) by a high $H_v$) and WTG (e.g. ensuring a fast MPPT process through increasing the bandwidth of the VSG's APC by a low $H_v$). Even, $H_v$ might be varied in an adaptive mode to improve transient stability of the power system following short circuit events. So, robust stability of the drive-train oscillations should be guaranteed so that power system operators can alter $H_v$ to enhance system stability. Regarding other eigenvalues, the $H_v$ increase moves the LF4 eigenvalue toward the right direction that indicating slower MPPT. Also, both the damped frequency and damping ratio of the LF3 eigenvalue (related to the inter-area oscillations) decrease as $H_v$ increases. Finally, the $H_v$ increase leads to the reduction in the damped frequency and damping ratio of the LF5 eigenvalue (related to the frequency regulation).

In contrast to $H_v$ change, the impact of variation of the $D_v$ on the LF6's stability is negligible because that variation hardly can impact the bandwidth of VSG's APC. In other words, the

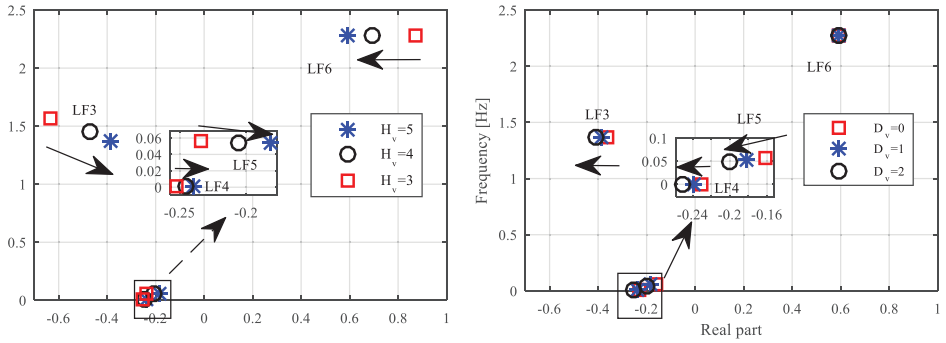


**FIGURE 5** Impact of variation of VSG's key parameters on the dominant eigenvalues of the test two machine power system comprised of uncompensated VSG-regulated type-4 WTG: (a) variation of $H_v$ and (b) variation of $D_v$

sensitivity of the discussed bandwidth to $H_v$ variation is higher than to the $D_v$ variation. Regarding other eigenvalues, the $D_v$ increase leads to a faster MPPT process by moving the LF4 eigenvalue toward the left direction. Moreover, the damping ratio of the LF3 eigenvalue increases as $D_v$ increases while its damped frequency is kept constant. Finally, the damped frequency and damping ratio of the LF5 eigenvalue decreases and increases respectively as the $D_v$ increases.

Nevertheless, to optimize the dynamics of system frequency, one should simultaneously design $H_v$ and $D_v$ say by increasing $H_v$ and $D_v$ to reduce the damped frequency and increase the damping ratio of the LF5 eigenvalue (to optimize frequency dynamics) while minimizing the speed reduction in the MPPT process. Also, with the simultaneous tuning of $H_v$ and $D_v$, it is possible to affect both the damped frequency and damping ratio of the LF3 eigenvalue in the desired direction. However, robust stability of drive-train dynamics should be ensured in advance. To support some statements, pole-zero analyses are also done; however, they are not reported to reduce pagination.

### 3.2.3 | Sensitivity analysis: Variation of wind power capacity penetration factor

The modal analysis is done again to study the impacts of a decrease in the capacity penetration factor of the wind turbines on the power system's eigenvalues. The rating of the thermal power plant and its step-up transformer (T1) is increased from 75 to 300 MW to reduce the capacity penetration factor of wind turbines to 20%. The constant impedance load values are also raised to 233.0750 MW and 75.9 MVAR.

From Figure 6, the reduction of the capacity penetration factor of the wind turbines [from 50% down to 20%] leads to slight relocation of the unstable LF6 eigenvalue toward the left side of the jω axis without changing the related damped frequency. This little impact was predictable from the results of the participation factor analysis that are reported in Table 1 because the state variables associated with the thermal power plant have low participation factors in the formation of the unstable eigenvalue. It is concluded that the identified undamped eigenvalue

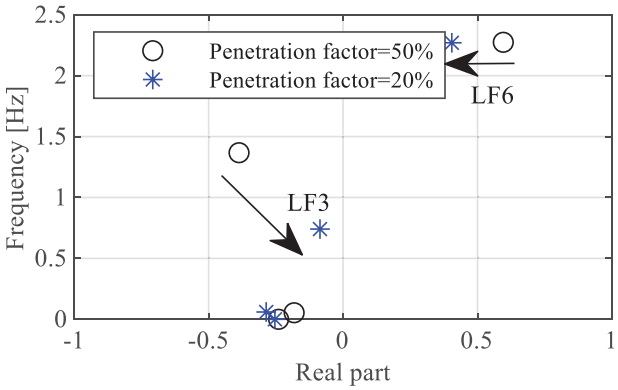


**FIGURE 6** Impact of penetration factor variation of wind power capacity on the dominant eigenvalues of the test two machine power system comprised of uncompensated VSG-regulated type-4 WTG

exists even if the installed capacity penetration factor of the wind turbines is reduced.

## 4 | COMPREHENSIVE ACTIVE TORSIONAL OSCILLATIONS DAMPER

So far, it is evident that drive-train dynamics of the VSG-regulated type-4 WTGs will always lead to a poorly damped eigenvalue in the integrated power system due to the lack of inherent damping offered by the considered WTG. The mentioned eigenvalue might be destabilized if $H_v$ takes low values. This section discusses the CA-TOD and its design and implementation approach to ensure the robust stability of drive-train oscillations.

### 4.1 | Adjusting the frequency and damping ratio of free-free torsional oscillations

In [19], it is possible to set both the natural frequency and the damping ratio of free-free torsional oscillations by including $K''_{sh}\theta_{sh} + D''_{tg}d\theta_{sh}/dt$ terms in the electrical torque of the PMSG,

see [22]. Inspired from methods proposed by references [7, 21], the presented CA-TOD introduces virtual shaft stiffness ($K^v_{sb}$) and virtual mutual turbine-generator damping factor ($D^v_{tg}$) to the WTG system. It is worth highlighting that PMSG's electrical torque should also contain $T_{ef}$ component for transmitting the wind power and stabilizing the DC voltage.

$$T_e = T_{ef} + K^v_{sb}\theta_{sb} + D^v_{tg}\frac{d\theta_{sb}}{dt},\ K^v_{sb} \geq 0,\ D^v_{tg} \geq 0 \tag{22}$$

In this context, Equation (22) is substituted in [19] to obtain the dynamic of the drive-train's shaft. Dynamic of $T_{ef}$ is assumed to be very slow due to the MPPT process; therefore, it has no impact on the CA-TOD.

$$\frac{d^2\theta_{sb}}{dt} + \left[D_{tg}\left(\frac{1}{2H_t}+\frac{1}{2H_g}\right) + \frac{\omega_{MelB}D^v_{tg}}{2H_g}\right]\frac{d\theta_{sb}}{dt}$$
$$+\left[\omega_{MelB}K_{sb}\left(\frac{1}{2H_t}+\frac{1}{2H_g}\right) + \frac{\omega_{MelB}K^v_{sb}}{2H_g}\right]\theta_{sb} = \frac{\omega_{MelB}T_t}{2H_t} - \frac{\omega_{MelB}T_{ef}}{2H_t} \tag{23}$$

From [23], the new natural frequency ($\omega^{sb}_{nc}$) and damping ratio ($\xi^{sb}_{nc}$) of the free-free torsional oscillations are given as below:

$$\omega^{sb}_{nc} = \sqrt{\frac{\omega_{MelB}K_{sb}}{2}\frac{H_t+H_g}{H_tH_g} + \frac{\omega_{MelB}K^v_{sb}}{2H_g}} \tag{24}$$

$$\xi^{sb}_{nc} = \left[\frac{D_{tg}}{4\omega^{sb}_n}\frac{H_t+H_g}{H_tH_g} + \frac{\omega_{MelB}D^v_{tg}}{4H_g\omega^{sb}_n}\right] \tag{25}$$

Comparing (20), (21), (24) and (25), the ability to set $\omega^{sb}_n$ and $\xi^{sb}_n$ at predefined values ($\omega^{sb}_{nc}$ and $\xi^{sb}_{nc}$) by adjustment of $K^v_{sb}$ and $D^v_{tg}$ values is clear, see (26) and (27).

$$K^v_{sb} = \left(2\left(\omega^{sb}_{nc}\right)^2 - \omega_{MelB}K_{sb}\frac{H_t+H_g}{H_tH_g}\right)\frac{H_g}{\omega_{MelB}} \tag{26}$$

$$D^v_{tg} = \left(\xi^{sb}_{nc} - \frac{D_{tg}}{4\omega^{sb}_{nc}}\frac{H_t+H_g}{H_tH_g}\right)\frac{4H_g\omega^{sb}_{nc}}{\omega_{MelB}} \tag{27}$$

According to (9)–(11), once the torsional oscillations of the shaft ($\theta_{sb}$) are stabilized, the torsional oscillations of the rotor and generator's speed will also be stabilized.

## 4.2 | Implementation of the CA-TOD

### 4.2.1 | The need for installation of an ESS and conceptual design

To implement the CA-TOD, damping torque formulated in [22] should be induced in the PMSG's electro-magnetic torque. Theoretically, this can be done by three approaches which were discussed in Section 1.2; however, none of them is technically feasible for VSG-regulated type-4 WTG. The first approach is to properly modulate $P^*_g$ of the VSG's APC in Figure 1 to extract suitable damping power from the DC link and in turn from the MSC and PMSG as the MSC would guarantee the power balance on the DC link by regulating its voltage. However, the VSG's APC should have low bandwidth to provide inertia effectively and therefore it cannot track reference damping power that would contain oscillatory elements with a frequency far above the bandwidth of the VSG's APC. The second approach is to properly modulate $v^*_{dc}$ of the MSC in Figure 1 to excite suitable damping torque in the PMSG because the DC voltage is regulated using the stored kinetic energy of the WTG. However, there exists a limited permissible margin for the value of $v^*_{dc}$ to ensure safety of DC capacitor and power switches and prevent overmodulation of MSC and GSC. Also, the phase delay of the DC voltage controller would drastically reduce the implementation's efficacy. The third approach is to add the suitable damping power as a feedforward term to the determined $P^*_s$ of the MSC. However, the high bandwidth of the DC voltage controller will effectively cancel this term due to its disturbance rejection feature.

Thus, it is proposed to introduce an ESS to the DC link of the WTG as shown in Figure 7, and inject the designed damping power in coordination with the DC voltage controller. The DC–DC converter can exchange the designed damping power between the ESS and the DC link (and the MSC in turn) following the damping power circulation path that is shown in Figure 7. Because the MSC maintains the DC link's power balance by regulating its voltage, the stabilizing power exchanged by the DC–DC converter will instantly flow from the MSC. In this context, a feedforward controller is also added to the output of the MSC's outer DC voltage control loop in Figure 1 that reflects the reference power of the ESS ($P^*_{ess}$) to minimize the perturbations on the DC voltage. Therefore, proper exchange of stabilizing power by the dc-dc converter will induce the desired damping torque in the PMSG. Nevertheless, MSC would have the capacity to exchange the stabilizing power by power converters since it is commonly oversized to draw over-rated active power from the PMSG under certain transient events and regulate PMSG's stator voltage by exchanging reactive current [36].

### 4.2.2 | Structure and model of the ESS

To implement the CA-TOD and induce the desired damping torque, an ESS with high power density, low energy density, and fast response is required to provide damping power and energy. Supercapacitor storage satisfies those requirements and due to its low volume, it can be located next to the WTG's power electronic converter [37]. In this research, the low-frequency model of the supercapacitor (shown in Figure 7) is adopted which is suitable for studying low-frequency oscillations of the power system.

As shown in Figure 7, a bidirectional boost converter comprised of two power switches ($S^1_b$ and $S^2_b$) and a series inductance ($L_b$) is utilized to connect the ESS to the DC link. $S^1_b$ and $S^2_b$ are switched in a complementary manner in a switching cycle and

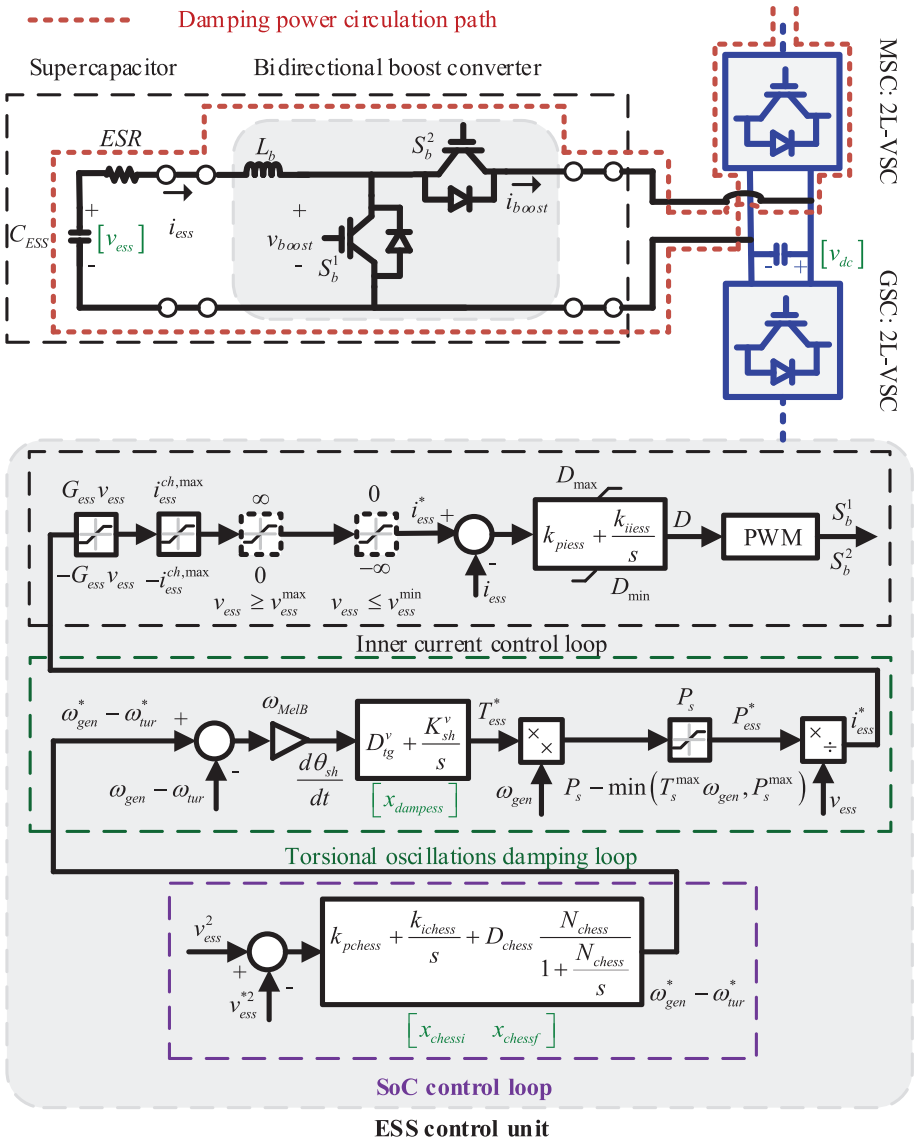


**FIGURE 7** Physical structure of the ESS unit and proposed controller loops to control supercapacitor's current, implement the CA-TOD, and regulate supercapacitor's SoC

the duty cycle of $S_b^1$ is $D$. Therefore, the averaged model of [28] is employed to represent the boost converter and relate its input and output voltages ($v_{boost}$ and $v_{dc}$) and currents ($i_{boost}$ and $i_{dc}$).

$$v_{boost} = (1-D)\, v_{dc};\ i_{boost} = (1-D)\, i_{ess} \tag{28}$$

Using [28], the electrical dynamics of the ESS unit can be represented by [29] and [30] to conduct EMT studies. In [29] and [30], $v_{ESS}$, $i_{ESS}$, $P_{ESS}$, and $C_{ESS}$ show the supercapacitor's voltage, current, power, and capacity respectively.

$$-v_{ess} + ESR \times i_{ess} + \frac{L_b}{\omega_b}\frac{di_{ess}}{dt} + (1-D)\, v_{dc} = 0 \tag{29}$$

$$i_{ess} = -C_{ess}\frac{dv_{ess}}{dt} \tag{30}$$

For small-signal studies, very fast current dynamics related to ESR and $L_b$ that are reported in [29] are neglected and the differential equation of (31) is used to model the voltage dynamic of the supercapacitor ($v_{ess}$) in the time domain ($P_{ess} = v_{ess}.i_{ess}$).

$$\frac{C_{ESS}}{\omega_{MelB}}\frac{dv_{ESS}^2}{dt} = -P_{ess} \tag{31}$$

### 4.2.3 | Proposed control strategy for the ESS

*Inner current controller*

The supercapacitor's current is controlled and injected into the DC link by the boost converter and its series inductance. The proposed controller for this converter is shown in Figure 7 where a current controller regulates the supercapacitor's current

($i_{ess}$). To design the current control loop, related dynamics that are reported in (29) should be considered. The high capacitance of the supercapacitor unit leads to an approximately constant $v_{ess}$ in the current control time scale. Also, $v_{dc}$ can be regarded as constant due to the action of MSC's DC voltage controller, slow evolution of $P_g^*$ due to WTG's inertia and low bandwidth of the VSG's APC unit in $P_g^*$ tracking, and summation of $P_{ess}^*$ with the output of the MSC's DC voltage controller in Figure 1. Therefore, [29] can be linearized as:

$$ESR \times \Delta i_{ess} + \frac{L_b}{\omega_b}\frac{d\Delta i_{ess}}{dt} - v_{dc0}\Delta D = 0 \tag{32}$$

From [32], $\Delta i_{ess}(s)/\Delta D(s)$ transfer function can be obtained as [33]. Using the optimum modulus method, a PI controller is tuned to obtain the closed-loop bandwidth of 280 Hz ( $k_{piess} = 0.0924$ and $k_{iiess} = 5.8038$) which is ten times less than the assumed switching frequency for the boost converter (2.8 kHz).

$$\frac{\Delta i_{ess}(s)}{\Delta D(s)} = \frac{(1/v_{dc0})}{(L_b/\omega_b)s + ESR} \tag{33}$$

For small-signal studies, current control dynamics are neglected.

*Torsional oscillations damping loop*

To implement the proposed damping torque in [22], which is $K_{sh}^v\theta_{sh} + D_{tg}^v d\theta_{sh}/dt$, first $d\theta_{sh}/dt$ is obtained by multiplying $\omega_{MelB}$ to the tracking error of $\omega_{gen}^* - \omega_{tur}^*$, see Figure 7. Then, $T_{ess}^*$ is obtained through processing $d\theta_{sh}/dt$ by $D_{tg}^v + K_{sh}^v/s$ PI controller. The stabilizing power reference ($P_{ess}^*$) is specified by multiplying the $T_{ess}^*$ by PMSG's speed ( $P_{ess}^* = T_{ess}^* \omega_{gen}$) to exchange suitable damping power with the PMSG. The stabilizing power reference is added to the output of the DC voltage controller in Figure 1 as a feedforward controller to increase the accuracy and reduce the DC voltage fluctuations and the phase delay caused by the DC-link voltage controller. Technical constraints associated with PMSG's torque and power are enforced while determining the ESS's reference power ($P_{ess}^*$) to ensure the system's security and avoid motor mode operation of the PMSG, see Figure 7. Finally, $i_{ess}^*$ is obtained by dividing the $P_{ess}^*$ by the $v_{ess}$.

$K_{sh}^v$ and $D_{tg}^v$ are the parameters designed following [26] and [27] to set the $\omega_{nc}^{sh}$ value ten times larger than the $BW_{VSG\text{-}APC}$ to prevent the propagation of torsional oscillations to the power system and set the $\xi_{nc}^{sh}$ value to 0.3 ( $\omega_{nc}^{sh} = 15.49\ Hz$, $K_{sh}^v = 51.65$ and $D_{tg}^v = 0.32$). $BW_{VSG\text{-}APC}$ can be calculated by deriving $\Delta P_g^*(s)/\Delta P_g(s)$ transfer function from Figure 3 using MATLAB software. In this sense, only the dynamics of the thermal power plant and related turbine-governing system, VSG, and network should be included and the frequency ($\omega_{BW}$) where $|\Delta P_g^*(j\omega_{BW})/\Delta P_g(j\omega_{BW})| = 1/\sqrt{2}$ should be found ($\omega_{BW}$ is 1.54 Hz in base case conditions). Related Bode diagrams are not shown to reduce the pagination. Changes in the power system structure and key control variables of the VSG's APC would not impact the adequate performance of the CA-TOD because the dynamics of the torsional oscillations and power system would be almost decoupled.

For small-signal studies, $P_{ess}^*$ is assumed to be $P_{ess}$ due to the perfect current control tracking. Also, governing equation for $P_{ess}^*$ is linearized as [34]. Note that steady-state exchanged stabilizing power by the ESS would be zero ( $T_{ess0}^* = 0$).

$$\Delta P_{ess}^* = T_{ess0}^* \Delta\omega_{gen} + \omega_{gen0}\Delta T_{ess}^* = \omega_{gen0}\Delta T_{ess}^* \tag{34}$$

*SoC control loop*

Finally, to regulate the supercapacitor's SoC, another cascaded control loop is proposed which regulates the square of the $v_{ess}^2$ around its reference value ($v_{ess}^{*2}$). Such regulation is carried out by implementing a PID controller and determining the $\omega_{gen}^* - \omega_{tur}^*$ speed difference, see Figure 7. The structure of the implemented PID controller is provided in [35] where the presence of a derivative component ($DN/(1+N/s)$) was necessary to introduce a positive phase to the cascade control framework and unstable plant dynamics ($\Delta v_{ess}^2(s)/[\Delta\omega_{gen}^*(s) - \Delta\omega_{tur}^*(s)]$), see Figure 8a. It is possible to integrate the model of the supercapacitor, CA-TOD, and SoC control loop in the systems linearized model (Figure 3) following the discussed small-signal models and assumptions.

The open loop's ($\Delta v_{ess}^2(s)/[\Delta v_{ess}^2(s) - \Delta v_{ess}^{*2}(s)]$) phase margin for the SoC control loop is selected to be 60° and the open loop's crossover frequency is reduced down to 1 rad/s to ensure stable (with low overshoot and ringing) but slow SoC regulation and prevent interference with the action of CA-TOD, see Figure 8b. Therefore, the eigenvalue related to drive-train oscillations should have a damped frequency and damping ratio close to the values targeted by $\omega_{nc}^{sh}$ and $\xi_{nc}^{sh}$ (this will be demonstrated in Section 5.1). Considering the linearized model of Figure 3 and the intended bandwidth and phase margin, the PID controller is tuned by using Simulink Control Design software MATLAB ($P = 0.013$, $I = 35e{-}5$, $D = 0.094$, $N = 2.706$).

$$P + \frac{I}{s} + D\frac{N}{1 + \frac{N}{s}} \tag{35}$$

## 5 | COMPENSATED WTG SYSTEM CONNECTED TO THE TWO MACHINE POWER SYSTEM: MODAL ANALYSIS

In this section, the performances of the CA-TOD and BPF-TOD in ensuring the robust stability of drive-train oscillations and the integrated power system are studied and compared concerning the variations of $H_v$, $D_v$, and parameter uncertainties of the drive-train.

### 5.1 | CA-TOD

The power system's eigenvalues when the aggregated VSG-regulated type-4 WTG is equipped with the CA-TOD are

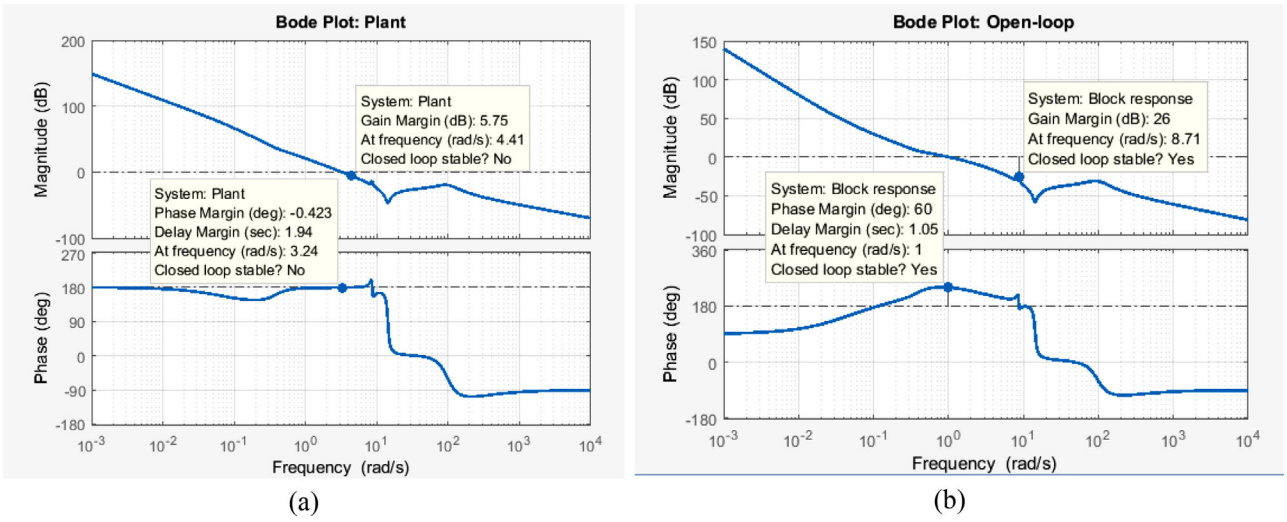


**FIGURE 8** Bode diagrams and minimum stability margins of (a) the plant transfer function $\Delta v_{ess}^2(s)/[\Delta\omega_{gen}^*(s) - \Delta\omega_{tur}^*(s)]$ and (b) open-loop transfer function $\Delta v_{ess}^2(s)/[\Delta v_{ess}^2(s) - \Delta v_{ess}^{*2}(s)]$ analyzed to design SoC for the capacitor

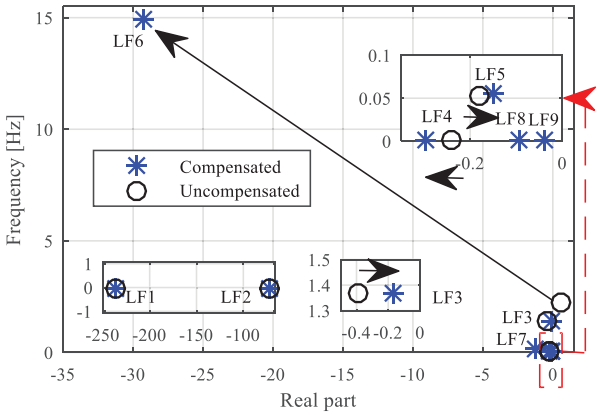


**FIGURE 9** Impacts of the CA-TOD on the eigenvalues of the test two machine power system comprised of VSG-regulated type-4 WTG

shown in Figure 9. The parameters of the ESS are reported in the appendix and the initial operating point is the case considered in Section 3.2.

According to the modal analysis, the compensated system consists of 13 eigenvalues compared to 9 eigenvalues for an uncompensated system. This shows that employing the CA-TOD and its associated ESS increases the number of the system's eigenvalues. LF1 and LF2 eigenvalues exist in both systems and have the same values. Characteristics of LF1-LF6 eigenvalues were described in Section 3.2. Results of PFA are presented in Table 2 for new as well as relocated eigenvalues.

Employment of the CA-TOD and proper design of $K_{sb}^{v}$ and $D_{tg}^{v}$ parameters have successfully resulted in reaching the natural frequency ($14.89/\sqrt{1-0.2986^2} = 15.60$ Hz) and the damping ratio (29.86%) of the torsional oscillations (LF6 eigenvalue) which are around the designed values (15.49 Hz and 30%), see Table 2. In this context, the CA-TOD did not destabilize any eigenvalue of the original WTG system. The involvement of $\omega_{gen}$, $\varkappa_{dampess}$, $\theta_{sb}$, and $v_{ess}$ state variables in this oscillatory eigenvalue clearly illustrates how the CA-TOD performs. It is also found that the state variables related to the VSG do not involve in the formation of LF6 because of increasing the frequency of torsional oscillations out of the bandwidth of VSG's APC. Nevertheless, the frequency and damping ratio of LF6 were 2.27 Hz and −4.16% in the case of uncompensated WTG, see Table 1; thus the improvement in the damping ratio of this oscillatory mode is significant.

Regarding newly emerged eigenvalues, the LF7 oscillatory mode is related to the dynamic interaction of the filter of ESS's SoC controller, the voltage of the supercapacitor, shaft's angle, speeds of generator and turbine, system's frequency, and CA-TOD. The contribution of these state variables in the formation of LF7 reflects the mechanism of the SoC control by the specification of $\omega_{gen}^* - \omega_{tur}^*$ speed difference, see Figure 7. Very low participation factor of the $\omega_{vsg}$ and $\omega_{sg}$ reveals that the dynamic of the SoC control is advantageously not dependent on the dynamics of the connected network; therefore, the characteristics of the LF7 eigenvalue are expected to be almost intact if the structure of the connected network changes. Finally, LF8 and LF9 eigenvalues are mainly related to the internal dynamics of the ESS's SoC controller and their value is primarily dependent on the related PID parameters due to the absence of participation of other state variables.

Regarding other eigenvalues, LF4 has moved a bit toward the left direction and $\varkappa_{chessf}$, $v_{ess}$, $\varkappa_{chessi}$ have newly gained participation and participation factors of $\varkappa_{gov}$, $\omega_{vsg}$, and $\omega_{sg}$ have been increased. This indicates that the proposed SoC controller slightly accelerates the decay mechanism of the MPPT process by impacting the power exchange between the WTG and ESS units as well as the WTG and the external network. Also, the LF3 (related to inter-area oscillations) and LF5 (related to the system's frequency) eigenvalues have moved slightly toward

**TABLE 2** Characteristics of eigenvalues of the test two machine power system comprised of CA-TOD compensated VSG-regulated type-4 WTG

| Eigenvalue | Frequency (HZ) | Damping ratio (%) | State variables with the highest participation factor |
|---|---|---|---|
| LF3 | 1.37 | 1.91 | $\theta_{vag-sg}(1),\omega_{sg}(0.5),\omega_{vsg}(0.5)$ |
| LF4 | 0 | 100 | $x_{chessf}(1),\omega_{tur}(0.96),x_{gov}(0.63),v_{ess}(0.55),\omega_{vsg}(0.38),\omega_{gen}(0.23),\omega_{sg}(0.07),x_{chessi}(0.03),$ |
| LF5 | 0.05 | 39.72 | $x_{gov}(1),\omega_{vsg}(0.68),\omega_{sg}(0.6),\omega_{tur}(0.41),\omega_{gen}(0.05)$ |
| LF6 | **14.89** | **29.86** | $\omega_{gen}(1),x_{dampess}(0.99),\theta_{sh}(0.02),v_{ess}(0.01)$ |
| LF7 | 0.15 | 79.35 | $x_{chessf}(1),v_{ess}(0.63),\theta_{sh}(0.61),\omega_{gen}(0.07),\omega_{tur}(0.06),\omega_{sg}(0.03),\omega_{vsg}(0.02),x_{dampess}(0.01)$ |
| LF8 | 0 | 100 | $x_{chessf}(1),x_{chessi}(0.38),\omega_{tur}(0.04)$ |
| LF9 | 0 | 100 | $x_{chessi}(1),x_{chessf}(0.37)$ |

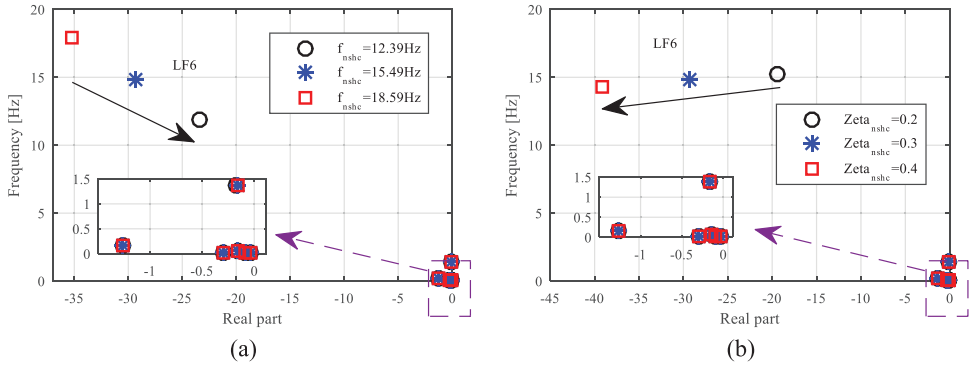


**FIGURE 10** Impact of variation of (a) $\omega_{nc}^{sh}$ and (b) $\xi_{nc}^{sh}$ on the dominant eigenvalues of the test two machine power system comprised of CA-TOD compensated and VSG-regulated type-4 WTG

the right direction but their frequency has not been changed suggesting that their damping ratio is slightly reduced. More importantly, $\theta_{sh}$, $\omega_{tur}$, and $\omega_{gen}$ have lost their participation in the formation of the LF3 eigenvalue thanks to the CA-TOD that has increased the natural frequency of torsional oscillations. This means that the proposed CA-TOD wipes off the reflected inter-area oscillations (in addition to the torsional oscillations) from the WTG's drive-train which further increases its lifetime.

In conclusion, with the help of a low-energy ESS, the presented CA-TOD successfully affected the LF6 eigenvalue (related to torsional oscillations) and had little impact on the other eigenvalues. Therefore, the presented CA-TOD and SoC controller had no adverse effect on the performance of the VSG controller, and the VSG can reliably utilize WTGs stored kinetic energy to participate in the frequency regulation of the power system

#### 5.1.1 | Sensitivity analysis: Variation of $\omega_{nc}^{sh}$ and $\xi_{nc}^{sh}$

The modal analysis is done again to study the impacts of reasonable variations of $\omega_{nc}^{sh}$ and $\xi_{nc}^{sh}$ on the integrated power system's eigenvalues. From Figure 10a, it is possible to successfully set the $\omega_{nc}^{sh}$ (related to the LF6 eigenvalue) at the intended value while keeping the $\xi_{nc}^{sh}$ almost constant. Note that $\omega_{nc}^{sh}$ should be calculated by $\omega_{nc}^{sh} = \omega_{dc}^{sh} / \sqrt{1 - \xi_{nc}^{sh2}}$ where $\xi_{nc}^{sh}$ is the damped frequency that is indicated on the $j\omega$ axis of the eigenvalue plot. Similarly, it can be inferred from Figure 10b that one can successfully set the $\xi_{nc}^{sh}$ (related to the LF6 eigenvalue) at the desired value while leaving the $\omega_{nc}^{sh}$ almost intact. Also, it is found that reasonable variations of $\omega_{nc}^{sh}$ and $\xi_{nc}^{sh}$ have no noticeable impact on other eigenvalues.

### 5.2 | Band-pass filter-based TOD

In this section, the modal analysis of the power system is done and it is assumed that the WTG system is compensated with BPF-based TOD. The aim is to establish a comparative study and analyze the effects of BPF-TOD on the integrated system's eigenvalues; however, the main focus will be on torsional oscillations. The system's parameters and initial operating point are the same as the ones adopted in Section 3.2.

To implement the BPF-TOD, at first, the natural frequency of torsional oscillations needs to be identified following the approach of Section 3.2 [9, 15]. That identification is challenging when the WTG is VSG-regulated due to the significant coupling between the two sides of the WTG's DC link. Moreover, the parameters of the VSG may be changed adaptively to support the grid frequency or the power system structure itself might change which will aggravate the challenge and might make BPF-TOD ineffective. Uncertainty of WTG's drive-train parameters

**TABLE 3** Characteristics of eigenvalues of the test two machine power system comprised of BPF-TOD compensated VSG-regulated type-4 WTG

| Eigenvalue | Frequency (HZ) | Damping ratio (%) | State variables with the highest participation factor |
|---|---|---|---|
| LF1 | 0 | 100 | $v_{dc}(1)$, $x_{vdc}(0.28)$, $x_{bpf2}(0.12)$, $\omega_{gen}(0.11)$, $x_{phc1}(0.01)$, $x_{phc2}(0.01)$ |
| LF2 | 0 | 100 | $x_{vdc}(1)x_{phc1}(0.05)$,$x_{phc1}(0.05)$,$x_{bpf2}(0.05)$,$\omega_{gen}(0.03)$,$v_{dc}(0.01)$ |
| LF6 | **2.22** | **3.00** | $\theta_{sh}(1)$,$\omega_{gen}(0.84)$,$v_{dc}(0.14)$,$\omega_{tur}(0.12)$,$x_{bpf1}(0.11)$,$x_{phc1}(0.10)$,$x_{phc2}(0.10)$,$x_{bpf2}(0.09)$,$\theta_{vsg-sg}(0.06)$,$\omega_{vsg}(0.05)$,$\omega_{sg}(0.01)$ |
| LF7 | 4.97 | 57.12 | $x_{bpf2}(1)$,$v_{dc}(0.76)$,$\omega_{gen}(0.71)$,$x_{phc1}(0.66)$,$x_{phc1}(0.66)$,$x_{bpf1}(0.15)$,$x_{vdc}(0.09)$,$\theta_{sh}(0.05)$ |

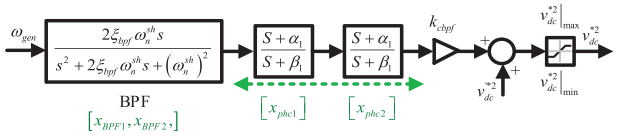


**FIGURE 11** Structure of BPF-based TOD ($\alpha_1 = 5.88, \beta_1 = 36.08, k_{cbpf} = -35, \xi_{bpf} = 0.8$)

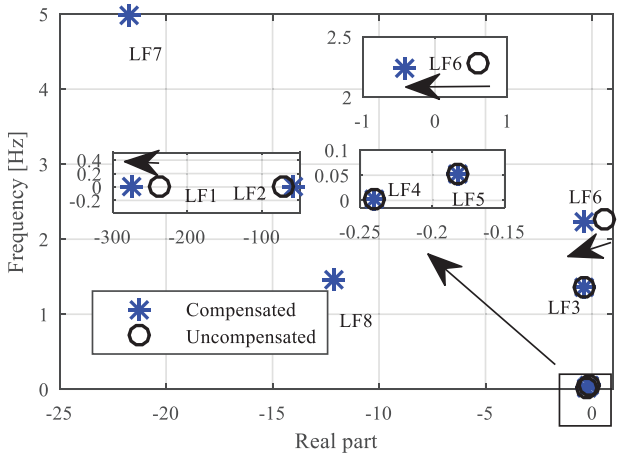


**FIGURE 12** Impacts of the BPF-TOD on the eigenvalues of the test two machine power system comprised of the VSG-regulated type-4 WTG

is another challenge. Then, a second-order BPF would extract the components related to the torsional oscillations from the $\omega_{gen}$. At the next step, a suitable phase should be injected to modulate the DC link's voltage amplitude and produce a stabilizing torque which should be in phase with the generator's speed [9, 15], see Figure 11. The BPF-based TOD can be easily included in the integrated system's linearized dynamic, see Figure 3; however, the saturated block should be removed.

According to the modal analysis, the compensated system has 13 eigenvalues. LF3, LF4, and LF5 eigenvalues in both compensated and uncompensated systems exit and have the same values and characteristics that were described in Section 3.2.4. The results of the PFA analysis are reported in Table 3 for newly emerged and relocated eigenvalues.

By employment of BPF-TOD, the damping ratio of the LF6 eigenvalue (related to the torsional oscillations) is increased from −4.16% in the uncompensated system to 3% in the compensated system. The frequency of torsional oscillations is decreased from 2.27 Hz in the uncompensated system to 2.22 Hz in the compensated system as a side effect. Participation of state variables $\boldsymbol{v_{dc}}$, $\boldsymbol{x_{BPF1}}$, $\boldsymbol{x_{BPF2}}$, $\boldsymbol{x_{phc1}}$, and $\boldsymbol{x_{phc2}}$ in the formation of the LF6 represents the mechanism of damping the torsional oscillations by the BPF-TOD which is based on modulation of the DC link voltage. The torsional oscillations' frequency is close to the bandwidth of VSG's active power controller; thus, $\boldsymbol{\theta_{vsg-sg}}$, $\boldsymbol{\omega_{vsg}}$ and $\boldsymbol{\omega_{sg}}$ state variables have retained their participation in the formation of LF6 eigenvalue. This undesirable fact implies the injection of torsional oscillations into the power system.

LF1 eigenvalue has moved left which implies that it will decay faster. LF1 is associated with the dynamic interaction of the WTG's DC link capacitor and its voltage controller. By comparing the participated state variables in the formation of LF1 in BPF-compensated and uncompensated systems, see Tables 3 and 1, it is found that the $\boldsymbol{x_{BPF2}}$, $\boldsymbol{\omega_{gen}}$, $\boldsymbol{x_{phc1}}$ and $\boldsymbol{x_{phc2}}$ state variables have gained participation. This is since the capacitive energy of the DC link is the primary source of providing stabilization power. On the other hand, the LF2 eigenvalue, which is associated with the interaction of the DC voltage controller and DC link's capacitor, has slightly moved to the right. By comparing the PFA reported in Tables 1 and 3, it is found that $\boldsymbol{x_{phc1}}$, $\boldsymbol{x_{phc2}}$, $\boldsymbol{x_{bpf2}}$, and $\boldsymbol{\omega_{gen}}$ state variables have gained participation in the formation of this eigenvalue in the compensated system. The gained participation is because BPA-TOD modulates the DC link's voltage reference to induce damping torque.

Also, the newly emerged LF7 eigenvalue is associated with the interaction of the BPF, DC-link capacitor, generator's speed, phase compensation units, DC voltage controller, and shaft angle. Limited space exists to increase the damping effect of the BPF-TOD and move the LF6 eigenvalue toward the left side through the increase of gain ($k_{cbpf}$) in Figure 11; because LF7 eigenvalue will move to the right direction and will eventually become unstable, see Figure 12 and 13.

## 5.3 | Comparative analysis

### 5.3.1 | Variation of VSG's key parameters ($H_v$ and $D_v$)

The modal analysis is done again to study the impacts of reasonable variations of VSG's key parameters on the performance of CA-TOD and BPF-TOD. From Figure 14a,b, variations of

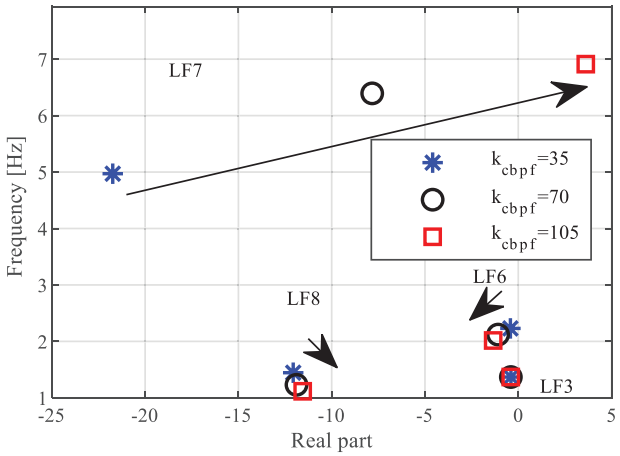


**FIGURE 13** Impact of increasing the $k_{cbpf}$ gain in BPF-TOD on dominant eigenvalues of the test two machine power system comprised of VSG-regulated type-4 WTG

$H_v$ and $D_v$ have almost no impact on the LF6 eigenvalue (that is related to torsional oscillations) as its damped frequency is far above the bandwidth of VSG's APC; therefore, CA-TOD can ensure its robust stability. It is noteworthy that the $H_v$ increase slightly accelerates the SoC recovery by relocating the LF7 eigenvalue to the left direction. Thanks to the robust stability of the drive-train oscillations, it is possible to optimally design $H_v$ and $D_v$ following the discussions given in Section 3.2.2 to affect the characteristics of the inter-area oscillation (related to LF3 eigenvalue) power system frequency (related to LF5 eigenvalue), and speed of MPPT process (related to LF4 eigenvalue).

From Figure 15a,b, BPF-TOD can only stabilize torsional oscillations (related to LF6 eigenvalue) when $H_v$ has low values. This is because of the limited stability margin provided by the BPF-TOD; therefore, detrimental interaction between the drive train, VSG's APC, and power system (that was described in Section 3.2.2) can destabilize the LF6 eigenvalue. On the other hand, variations of the $D_v$ have almost no impact on the stability of the LF6 eigenvalue due to the reasons discussed in Section 3.2.2. Therefore, it is not possible to optimally tune $H_v$ and $D_v$ to improve power system dynamics.

### 5.3.2 | Impacts of drive-train parameter uncertainty

In this subsection, the objective is to analyze the effect of parameters' uncertainty in WTG's drive-train on the performance of the CA-TOD and BPF-TOD. Therefore, the $H_t$ and $H_g$ parameters are increased by 10% and $K_{sh}$ parameter is decreased by 10%. The $D_{tg}$ parameter is kept unchanged due to its very low initial value. These changes will increase $\omega_n^{sh}$ and $\xi_n^{sh}$ according to (20) and (21). In consequence, BPF-TOD will no longer be able to properly derive the oscillatory component of the PMSG's speed. Hence, its performance is significantly reduced but the WTG system is still stable, see Figure 16b. The damping effect provided by the BPF-TOD to the torsional oscillations is limited; thus, parameter uncertainty might destabilize the integrated system if further parameter uncertainty is assumed.

On the other hand, the CA-TOD can prove robust stability because it provides considerable damping to the torsional oscillations (LF6 eigenvalue). Thus, the stability margin is still high even in the presence of the parameter uncertainty, see Figure 16a. However, due to the parameter uncertainty, the resulted natural frequency and damping ratio of torsional oscillations have deviated from the designed values.

## 6 | ELECTRO-MAGNETIC TRANSIENT SIMULATION RESULTS

### 6.1 | Test two machine power system: wind speed decrease

The EMT model of the two-machine integrated power system is developed in the MATLAB/Simulink platform to assess and compare the dynamic performance and robustness of the CA-TOD and BPF-TOD and to authenticate to results of small signal studies. In the simulations, the wind speed is stepped down at $t = 20$ s from 10.68 to 9.68 m/s.

#### 6.1.1 | Performance evaluation of the CA-TOD

The transient dynamics related to the critical variables of the WTG system and its connected network are shown in Figure 17. The unstable uncompensated system is simulated till $t = 27$ s and the related results are shown as distinct subplots to make the figures legible.

Considering the uncompensated WTG, the turbine-generator speeds start to decrease as the aerodynamic torque decreases instantly; however, the electrical torque decreases slowly. It is because PMSG's electric torque and power depend on the GSC's active power which itself is regulated by the VSG unit. The VSG's APC has low bandwidth and its reference varies slowly because of the adopted MPPT process and the large inertia of the WTG. Nevertheless, PMSG's electrical torque will eventually decrease following the system's dynamics. Drive-train's torsional oscillations are excited due to the wind speed change. The presence of these oscillations at the generator's speed and shaft's torque will reduce their lifetime, see Figure 17d,e. The frequency of those unstable torsional oscillations is 2.27 Hz and verifies the findings of the modal analysis. These torsional oscillations are also reflected in the electrical output power of the GSC and injected into the grid due to the action of the VSG's APC which is in charge of the MPPT, see [17]. Therefore, the power system frequency has been destabilized, see Figure 17j. Note that inter-area oscillations are also excited due to the wind speed decrease, and they are reflected on the GSC's active power and then WTG's drive-train according to the predictions of Section 3.2; however, their magnitude is not noticeable in comparison with the magnitude of unstable torsional oscillations.

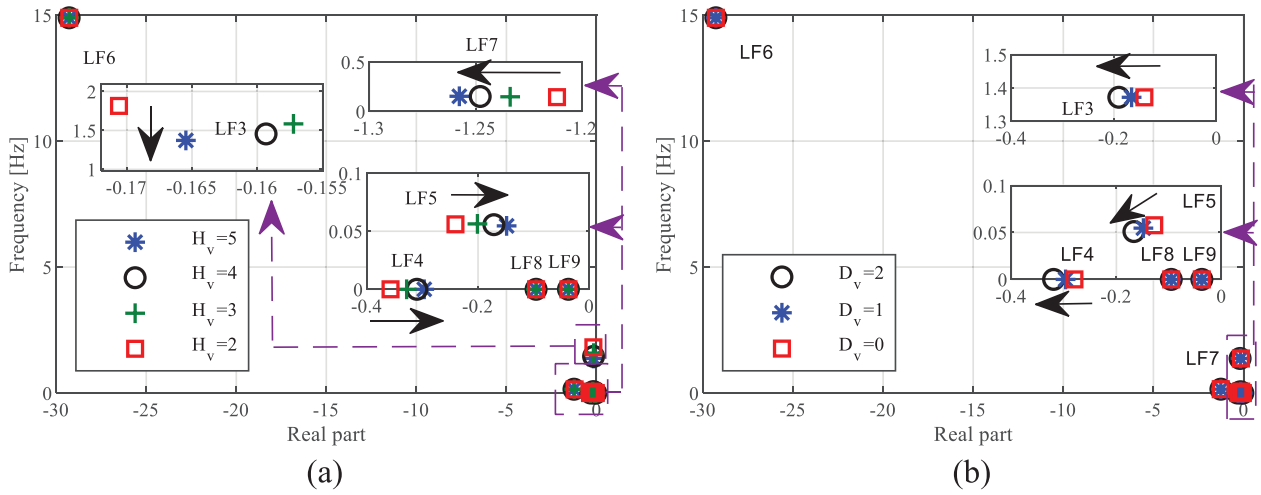


**FIGURE 14** Impact of variation of $H_v$ and $D_v$ the dominant eigenvalues of the test two machine power system comprised of CA-TOD compensated and VSG-regulated type-4 WTG: (a) variation of $H_v$ and (b) variation of $D_v$

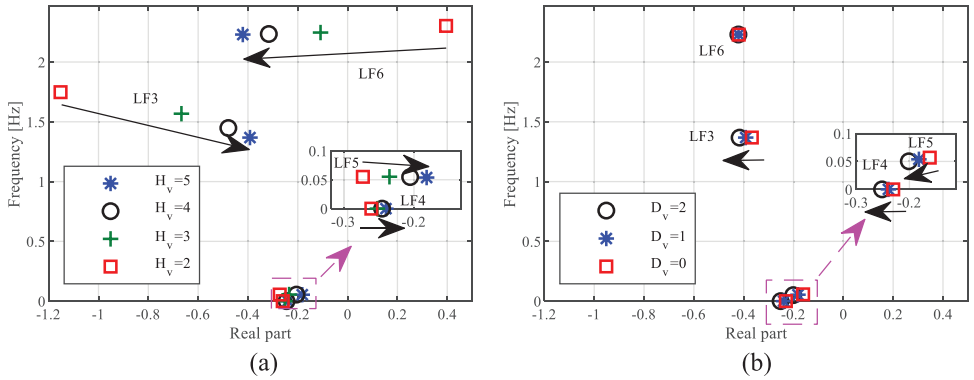


**FIGURE 15** Impact of variation of $H_v$ and $D_v$ on the dominant eigenvalues of the test two machine power system comprised of BPF-TOD compensated and VSG-regulated type-4 WTG: (a) variation of $H_v$ and (b) variation of $D_v$

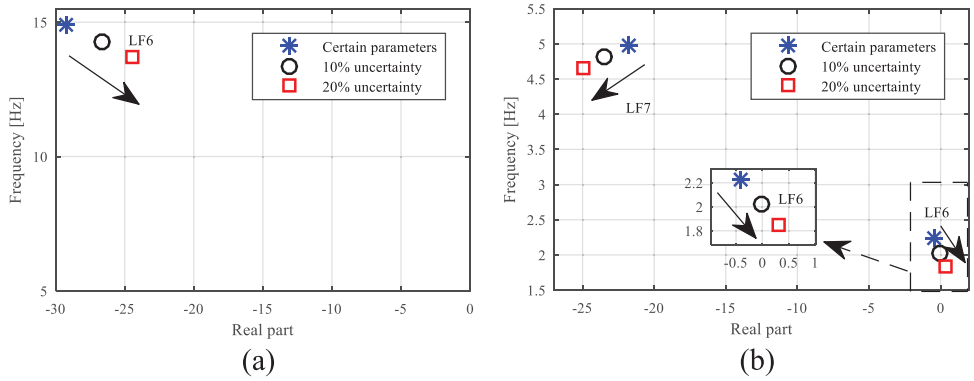


**FIGURE 16** Impacts of parameter uncertainties in WTG's drive-train on the stability of the integrated two machine power system inclusive of an aggregated WTG system compensated with (a) CA-TOD and (b) BPF-TOD

Regarding the CA-TOD, all the system's variables have been changed following the wind speed decrease; however, torsional oscillations are successfully stabilized, see Figure 17d,e, which verifies the results of the modal analysis. It is also clear that the ESS has injected the required damping power first milliseconds of the transient regime, see Figure 17g, which has been reflected in the PMSG's power, see Figure 17c, and thus suitable stabilizing electrical torque has been induced, see

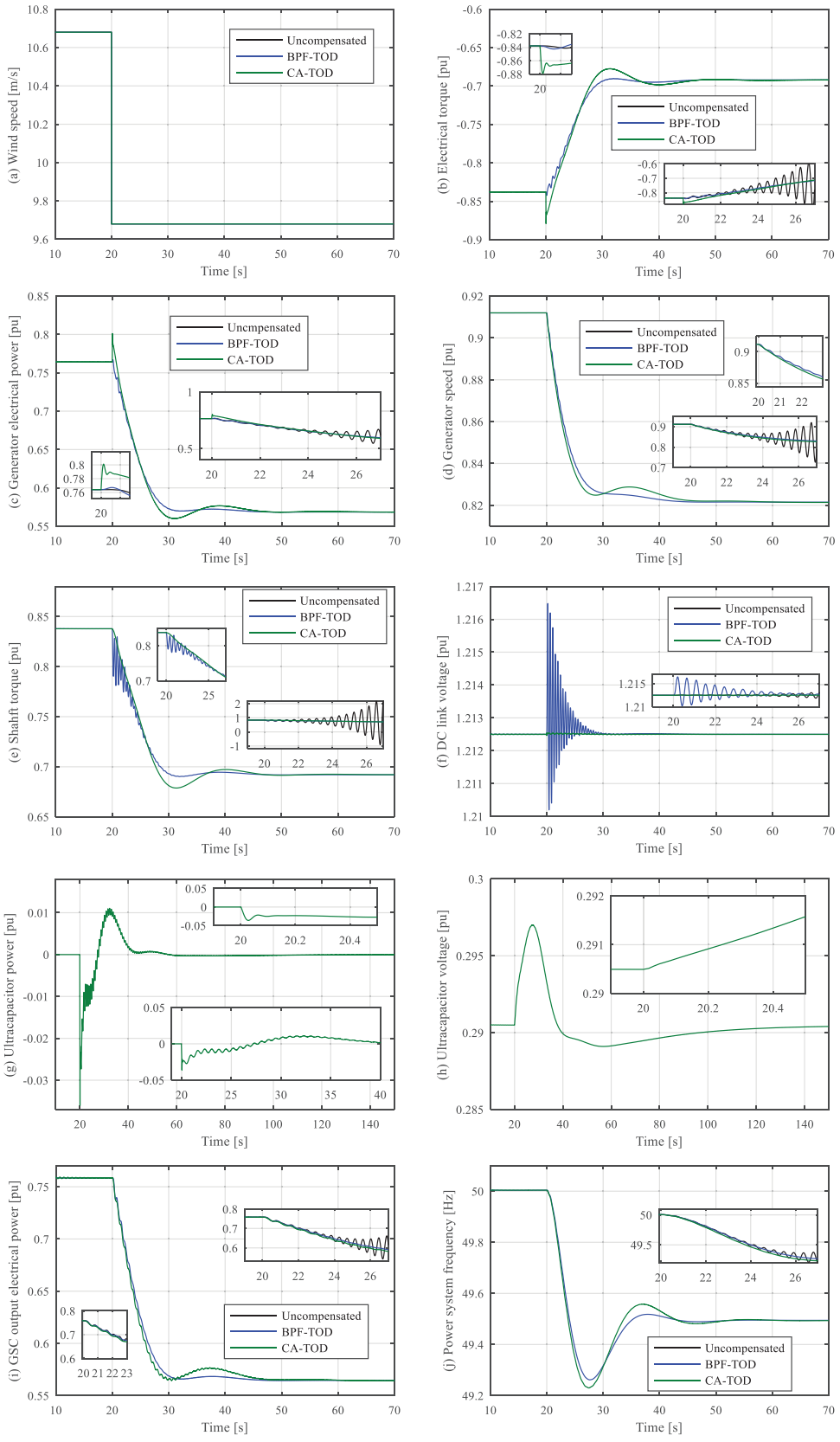


**FIGURE 17** Transient response of the VSG-regulated type-4 WTG to wind speed change

Figure 17b, that will increase the drive-train's lifetime. Using the proposed feedforward controllers, fluctuations of the DC link voltage are negligible, see Figure 17f. Due to the significant increase in the frequency of the torsional oscillations, the output power of the GSC (Figure 17i) is free of these torsional oscillations which is advantageous for maintaining the power system stability. Also, the SoC controller of the ESS has recovered the supercapacitor's voltage, see Figure 17h. The time frame of the charge recovery was much larger than the time frame of the torsional oscillations and the MPPT process has completed successfully. Inter-area oscillations are reflected on the GSC's active power, see Figure 17i. However, the supercapacitor has absorbed all the reflected inter-area oscillation on the drive-train (see Figure 17g) and has made the shaft torque and other state variables of the drive-train free of both torsional and inter-area oscillations as a clear advantage, see Figure 17e. Thus, the adequate performance of the CA-TOD is demonstrated.

### 6.1.2 | Comparative analysis

To conduct a comparative analysis, the integrated system was simulated again and the WTG system was compensated by the BPF-based TOD. Torsional oscillations are stabilized by modulation of the DC-link's voltage amplitude, see Figure 17e,f; however, in comparison with the CA-TOD, it takes a long time to stabilize the torsional oscillations which was predicted by the small-signal analysis. Also, the BPF-TOD cannot prevent the reflection of the inter-area oscillations on the drive-train's state variables. Moreover, the frequency of torsional oscillations is almost unchanged and is close to the bandwidth of the VSG's APC. Therefore, the torsional oscillations can be reflected in the GSC's output power to a certain extent, which is undesirable.

Predictions of Sections 5.1 and 5.2 regarding that the (unlike BPF-TOD) CA-TOD slightly decreases the damping ratio of the frequency regulation process and inter-area oscillations are also verified by Figure 17i,j. However, thanks to the robust stability provided by the CA-TOD to the drive-train, the discussed damping ratio can be easily increased by optimum tuning of $H_v$ and $D_v$.

### 6.1.3 | Impacts of drive-train parameter uncertainty

In this section, the scenario of drive-train's parameter uncertainty is discussed. Simulation results related to BPF-TOD and CA-TOD are presented in Figure 18a,b. From Figure 18a, the performance of BPF-TOD has been degraded significantly with uncertainty level increase, and finally, the system has been destabilized due to the reasons described in Section 5.3.2. However, from Figure 18b and due to the justifications explained in Section 5.3.2, damping of torsional oscillations remains perfect when the CA-TOD is adopted.

## 6.2 | 75 MW wind farm connected to power system: Load increase

In this section, a detailed 75 MW wind farm comprised of 15 numbers of 5 MW WTGs is connected to a modified P.M. Anderson power system, see Figure 19. Wake effect and internal cablings and transformers of the wind farm are considered as per modeling and parameters reported in [5, 38]. The power system is downscaled, modelled, and parameterized following the guidelines of [26, 35] to reach a 50% penetration factor for the capacity of the installed wind farm. Specifically, the EMT models of the thermal power plants are developed following the assumptions made in Section 2.3. The purpose is to evaluate the dynamic performance of the CA-TOD and BF-TOD and verify the general predictions of the conducted modal analysis when a detailed wind farm is connected to a realistic power system. Over the simulations, the load of bus 5 is increased at $t = 40$ s by 11.8 MW, and the results related to the WTG.ST1:4 (see Figure 19) are provided in the simulations.

At this stage, consider the base case: $H_v = 8$ and $D_v = 1$. After generation-consumption imbalance, the power system's frequency starts to decrease and oscillate, see Figure 20a-right and left columns- and the WTGs provide inertial frequency support, see Figure 20b-right and left columns. Short-term active power increase by WTGs has resulted in a decrease in their speed and excitation of their drive-train dynamics, see Figure 20d-right and left columns-. Both CA-TOD and BPF-TOD were able to stabilize the torsional oscillations, however, the CA-TOD accomplished the stabilization process more quickly, see Figure 20d-right and left columns-. Damping power was absorbed from the ESS in the first milliseconds of the transient regime and then the ESS unit absorbed all the inter-area oscillations reflected by the GSC; therefore, the generator's speed is free from both torsional and inter-area oscillations, see Figure 20c,d-right column-. On the other hand, the BPF-TOD cannot remove the reflected inter-area oscillations on the drive-train and has inferior performance (compared to CA-TOD) in stabilizing the torsional oscillations. These findings further verify the effective and superior performance of the CA-TOD and general predictions of the modal analysis presented in Sections 5.1 and 5.2 in a realistic power system.

### 6.2.1 | Sensitivity analysis: Variation of VSG's key parameters ($H_v$ and $D_v$)

From Figure 20 (left column), the BPF-TOD can stabilize the integrated system when the $H_v$ value is low and therefore the bandwidth of the VSG' APC and detrimental interactions of the torsional oscillations and the external network are lower, refer to Section 3.2.2. However, as $H_v$ decreases torsional oscillations grow and finally destabilize the system's frequency by pouring the torsional oscillations by the action of the GSC which is in line with general predictions of Section 5.3.1. However, stability limits are further reduced because the two-machine power system was found to be stable when $H_v$ was 3.6, see Figure 15a.

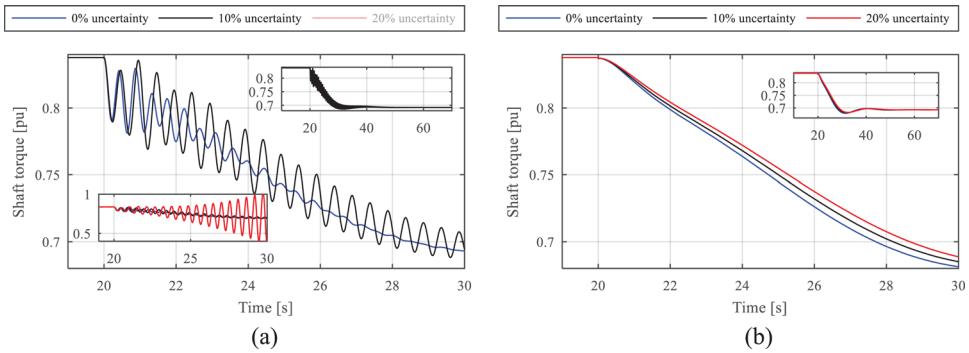


**FIGURE 18** Transient response of the WTG to wind speed change in the presence of the drive-train's parameter uncertainty: (a) BPF-TOD and (b) CA-TOD

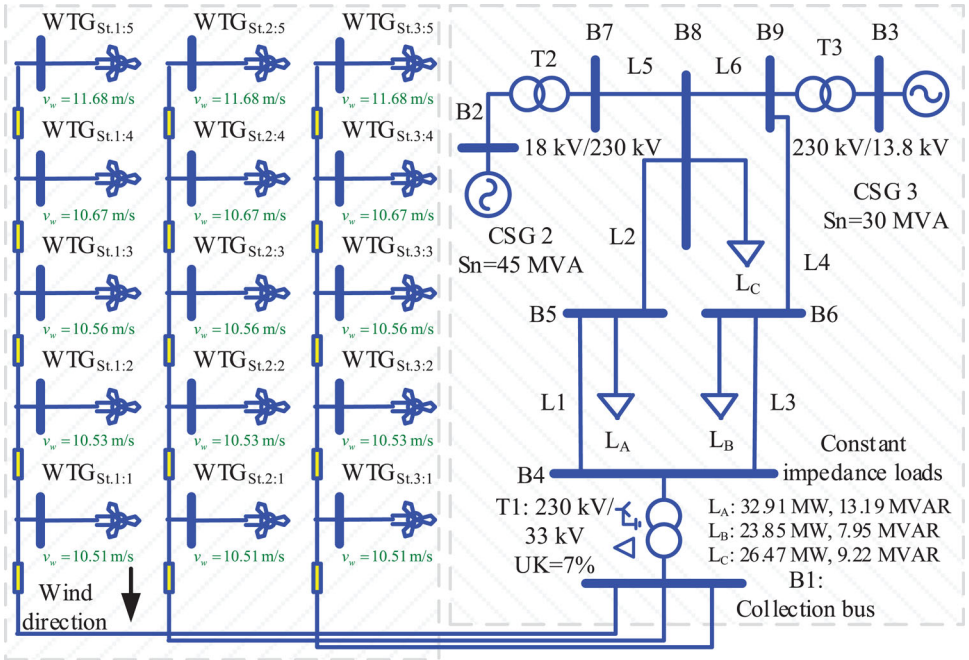


**FIGURE 19** A detailed 75 MW wind farm connected to downscaled P.M. Anderson power system

This is because of the damping mechanism of the BPF-TOD which highly depends on proper knowledge of torsional oscillations frequency, key parameters of the VSG, and the structure of the external network, refer to Section 5.3.1. On the other hand, it is found from Figure 20 (right column) that CA-TOD can ensure robust stability of the realistic power systems concerning the variations of the $H_v$ thanks to its damping mechanism, refer to Section 5.3.1.

Also, it is clear from Figure 21 that variations of the $D_v$ have no significant impact on the capability of the BPF-TOD and CA-TOD in the stabilization of the drive-train oscillations. It is mainly because variations of the $D_v$ have little effect on the bandwidth of the VSG' APC and the level of interactions between torsional and power system dynamics, refer to Section 3.2.2. Comparison of the frequency dynamics and GSC's power in the left and right columns of Figure 21 confirms the general predictions of Sections 5.1 and 5.2 that the CA-TOD slightly reduces the damping ratio of the frequency oscillations in comparison with the BPF-TOD. However, thanks to the robust drive-train stability attained by the CA-TOD, it is possible to optimally tune $H_v$ and $D_v$ to significantly improve the stability of the power system frequency.

## 7 | CONCLUSIONS

In this study, the stability of power systems comprised of thermal and VSG-regulated type-4 WTGs was analyzed, characterized and multi mass-spring models were adopted to model WTGs drive-train dynamics. An unstable eigenvalue was found that determines the power system's stability and was related to the WTGs' drive-train dynamics and its interaction with the dynamics of the VSG and external network. The origin of the

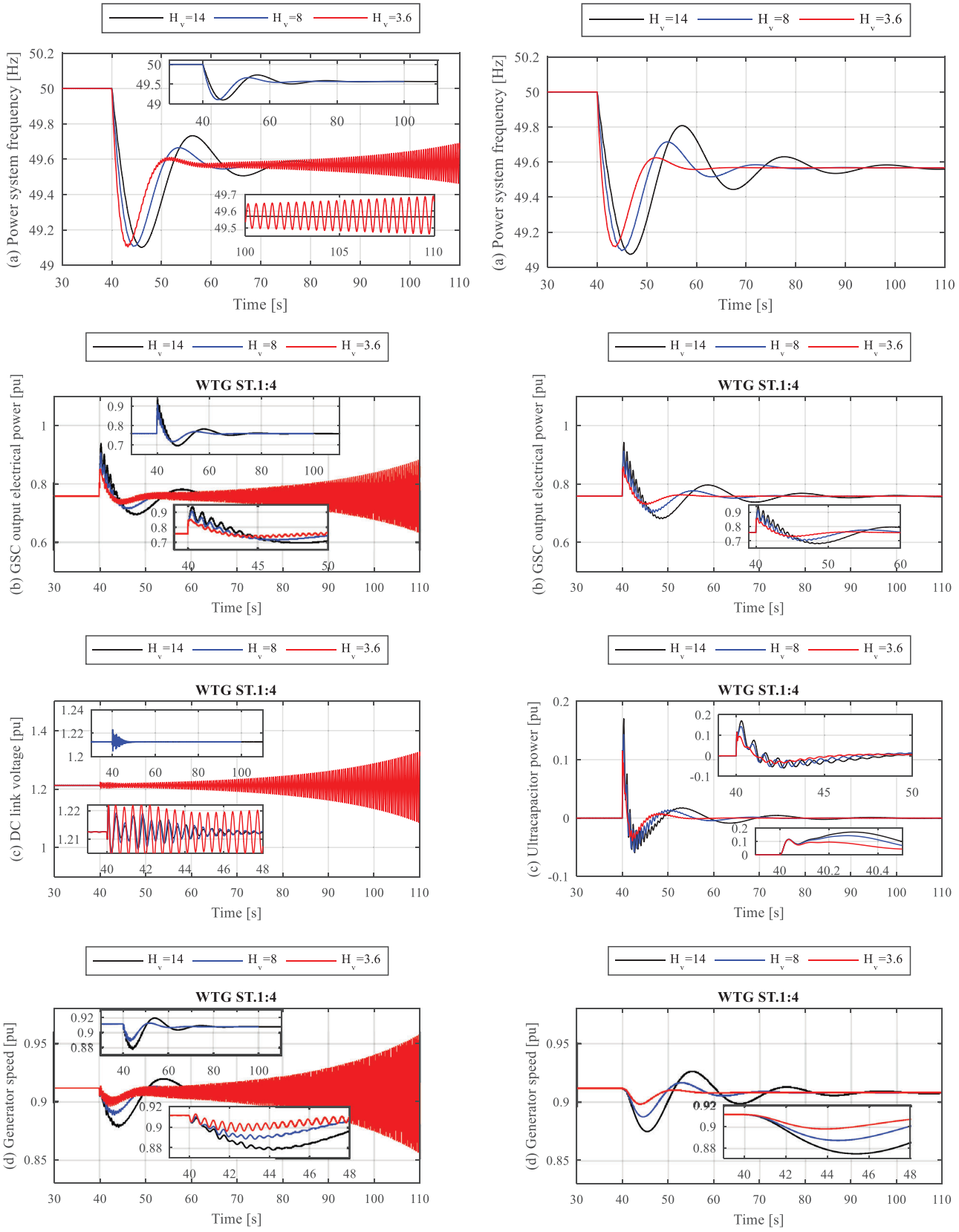


**FIGURE 20** Impact of variation of $H_v$ on the transient response of the test P.M. Anderson power system comprised of a detailed 75 MW wind farm ($D_v = 1$): (left column) application of BPF-TOD and (right column) application of CA-TOD

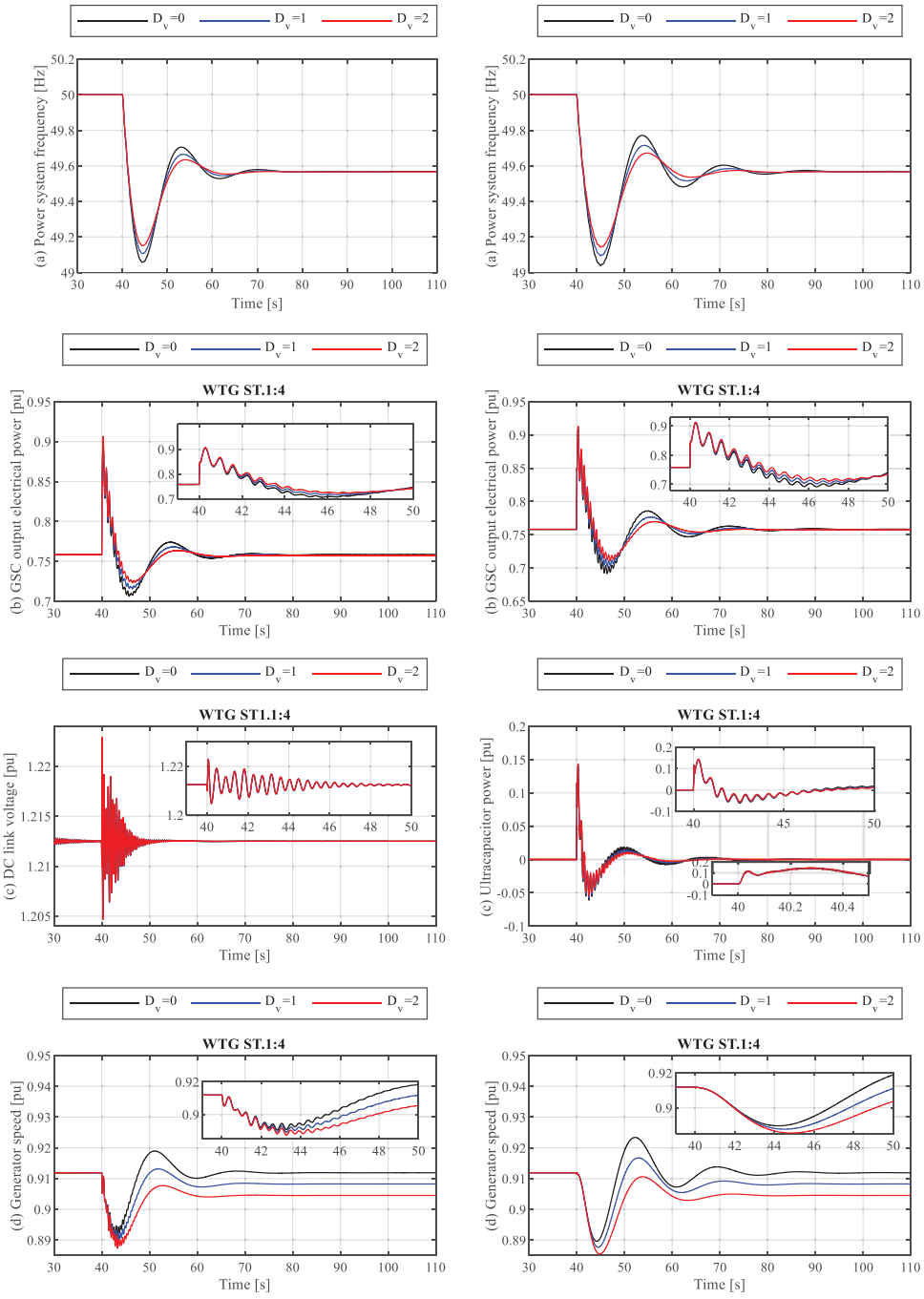


**FIGURE 21** Impact of variation of $D_v$ on the transient response of the test P.M. Anderson power system comprised of a detailed 75 MW wind farm ($H_v = 8$): (left column) application of BPF-TOD and (right column) application of CA-TOD

instability was found to be the absence of inherent damping in the drive-train. A reduction in $H_v$ value was found to further destabilize the unstable eigenvalue while variation in $D_v$ value was found to have a negligible impact on the unstable eigenvalue. The frequency of WTGs' torsional oscillations was within the bandwidth of the VSG's active power controller; therefore, they propagated to the power system. Therefore, inertia provision by VSG-regulated type-4 WTG can lead to WTG/power system instability rather than enhancing frequency stability. Accordingly, power system stability analysis should be done by modeling drive-train dynamics of frequency-responsive WTGs. The presented CA-TOD was able to increase the frequency of torsional oscillations out of the VSG's bandwidth and could significantly increase the damping of torsional oscillations without destabilizing other systems' eigenvalues. The presented CA-TOD ensures superior robust stability compared to the traditional BPF-based TOD when $H_v$ has a low value and when the drive-train parameters are subjected to uncertainty. It was also

discussed that the proposed SoC controller can operate properly without impairing the performance of the CA-TOD and impacting other system dynamics as the bandwidth of the SoC controller was selected to be significantly low. Modal and EMT studies on an aggregated wind farm connected to a single bus power system and EMT studies on a detailed 75 MW wind farm connected to a multi-machine power system demonstrated the superior efficiency of the proposed active damper/controllers and attested to the authenticity of the drawn analysis. Future work is suggested to analyze the eigenvalues of a large and multi-area power system inclusive of VSG-regulated type-4 WTGs and grasp more insights into the interaction of the drive train dynamics and the rest of the power system and evaluate the effective performance of the presented CA-TOD and SoC controller.

## NOMENCLATURE

| | |
|---|---|
| $\theta_{vsg-sg}$ | Differential angle of virtual and actual synchronous generators |
| $\omega_{gen}$ | Rotational speed of generator |
| $\omega_{sg}$ | Frequency of synchronous generator |
| $\omega_{tur}$ | Rotational speed of turbine |
| $\omega_{vsg}$ | Frequency of virtual synchronous generator |
| $v_{dc}$ | DC link voltage |
| $v_{ess}$ | Supercapacitor's voltage |
| $x_{BPF1}$, $x_{BPF2}$ | State variables of the band-pass filter |
| $x_{chessf}$ | State variables of supercapacitor's voltage controller (filter part) |
| $x_{chessi}$ | State variables of supercapacitor's voltage controller (integral part) |
| $x_{dampess}$ | State variable of supercapacitor's torsional oscillations damping loop |
| $x_{phc1}$, $x_{phc2}$ | State variables of the phase compensator |
| $x_{vdc}$ | State variable of DC voltage controller |
| $\theta_{sh}$ | Torsional angle of drive-train's shaft |

## AUTHOR CONTRIBUTIONS

M.B.: Conceptualization; Formal analysis; Funding acquisition; Investigation; Methodology; Project administration; Supervision; Writing – review and editing

## ACKNOWLEDGEMENT

This work was supported by the Collaborative Research Grant (CRP) of Nazarbayev University, (Project no. 021220CRP0322)

## CONFLICT OF INTEREST

The authors declare no conflict of interest.

## DATA AVAILABILITY STATEMENT

The data that support the findings of this study are available from the corresponding author upon reasonable request.

## ORCID

*Mehdi Bagheri* https://orcid.org/0000-0002-8078-9173

## REFERENCES

1. Bastiani, B.A., de Oliveira, R.V: Adaptive MPPT control applied to virtual synchronous generator to extend the inertial response of type-4 wind turbine generators. Sustainable Energy, Grids Networks 27, 100504 (2021)
2. Rakhshani, E., Rodriguez, P: Inertia emulation in AC/DC interconnected power systems using derivative technique considering frequency measurement effects. IEEE Trans. Power Syst. 32(5), 3338–3351 (2017)
3. Li, D., Zhu, Q., Lin, S., Bian, X.Y: A self-adaptive inertia and damping combination control of VSG to support frequency stability. IEEE Trans. Energy Convers. 32(1), 397–398 (2017)
4. Xi, J., Geng, H: Decoupling control scheme for VSG-WPPs to participate in grid frequency response. IEEE Trans. Ind. Appl. 55(6), 6368–6375 (2019)
5. Yazdi, S.S.H., Milimonfared, J., Fathi, S.H., Rouzbehi, K: A Comprehensive VSG-based onshore FRT control strategy for OWFs with VSC-MT-HVDC transmission. IEEE Access 9, 155788–155804 (2021)
6. Geng, H., Xu, D., Wu, B., Yang, G: Comparison of oscillation damping capability in three power control strategies for PMSG-based WECS. Wind Energy 14(3), 389–406 (2011)
7. Liu, J., Zhou, F., Zhao, C., Wang, Z: Mechanism analysis and suppression strategy research on permanent magnet synchronous generator wind turbine torsional vibration. ISA Trans. 92, 118–133 (2019)
8. Geng, H., Xu, D., Wu, B., Yang, G: Active damping for PMSG-based WECS With DC-link current estimation. IEEE Trans. Ind. Electron. 58(4), 1110–1119 (2011)
9. Hansen, A.D., Michalke, G: Modelling and control of variable-speed multi-pole permanent magnet synchronous generator wind turbine. Wind Energy 11(5), 537–554 (2008)
10. Arani, M.F.M., Mohamed, Y.A.I: Analysis and damping of mechanical resonance of wind power generators contributing to frequency regulation. IEEE Trans. Power Syst. 32(4), 3195–3204 (2017)
11. Alizadeh, O., Yazdani, A: A strategy for real power control in a direct-drive PMSG-based wind energy conversion system. IEEE Trans. Power Delivery 28(3), 1297–1305 (2013)
12. Geng, H., Xu, D: Stability analysis and improvements for variable-speed multipole permanent magnet synchronous generator-based wind energy conversion system. IEEE Trans. Sustainable Energy 2(4), 459–467 (2011)
13. Rahimi, M., Beiki, A: Efficient modification of the control system in PMSG-based wind turbine for improvement of the wind turbine dynamic response and suppression of torsional oscillations. Int. Trans. Electr. Energy Syst. 28(8), e2578 (2018)
14. Beiki, A., Rahimi, M: An efficient sensorless approach for energy conversion enhancement and damping response improvement in permanent magnet synchronous generator (PMSG) based wind turbines. Int. Trans. Electr. Energy Syst. 29(1), e2684 (2019)
15. Jauch, C: Transient and dynamic control of a variable speed wind turbine with synchronous generator. Wind Energy 10(3), 247–269 (2007)
16. Licari, J., Ugalde-Loo, C.E., Ekanayake, J.B., Jenkins, N: Comparison of the performance and stability of two torsional vibration dampers for variable-speed wind turbines. Wind Energy 18(9), 1545–1559 (2015)
17. Laubrock, M., Woldmann, T.P., Bilges, S.: "Method for the active damping ofthe drive train in a wind energy plant," U.S. Patent 7501798B2 Patent, Mar. 10, 2009
18. Chen, J., Chen, J., Gong, C: On optimizing the aerodynamic load acting on the turbine shaft of PMSG-based direct-drive wind energy conversion system. IEEE Trans. Ind. Electron. 61(8), 4022–4031 (2014)
19. Jun-Keun, J., Seung-Ki, S: Kalman filter and LQ based speed controller for torsional vibration suppression in a 2-mass motor drive system. IEEE Trans. Ind. Electron. 42(6), 564–571 (1995)
20. Licari, J., Ugalde-Loo, C.E., Ekanayake, J.B., Jenkins, N: Damping of torsional vibrations in a variable-speed wind turbine. IEEE Trans. Energy Convers. 28(1), 172–180 (2013)
21. Kambrath, J.K., Khan, M.S.U., Wang, Y., Maswood, A.I., Yoon, Y: A novel control technique to reduce the effects of torsional interaction in wind turbine system. IEEE J. Emerging Sel. Top. Power Electron. 7(3), 2090–2105 (2019)

22. Alizadeh, O., Yazdani, A: A control strategy for power regulation in a direct-drive WECS with flexible drive-train. IEEE Trans. Sustainable Energy 5(4), 1156–1165 (2014)
23. Li, M., Zhang, J., Wu, C., Zhu, R., Chen, W., Duan, C., et al. Effects of silicone oil on stiffness and damping of rubber-silicone oil combined damper for reducing shaft vibration. IEEE Access 8, 218554–218564 (2020)
24. Kunjumuhammed, L.P., Pal, B.C., Gupta, R., Dyke, K.J: Stability analysis of a PMSG-based large offshore wind farm connected to a VSC-HVDC. IEEE Trans. Energy Convers. 32(3), 1166–1176 (2017)
25. Liu, H., Li, M., Liu, L., Shi, J: Frequency trajectory planning-based transient frequency regulation strategy for wind turbine systems. IEEE J. Emerging Sel. Top. Power Electron. 10(4), 3987–4000 (2022) https://doi.org/10.1109/JESTPE.2021.3113822
26. Heidary Yazdi, S.S., Milimonfared, J., Fathi, S.H., Rouzbehi, K., Rakhshani, E: Analytical modeling and inertia estimation of VSG-controlled Type 4 WTGs: Power system frequency response investigation. Int. J. Electr. Power Energy Syst. 107, 446–461 (2019)
27. Malekpour, M., Kiyoumarsi, A., Gholipour, M: Analytical system frequency response model with virtual synchronous wind turbines. IET Gener. Transm. Distrib. 15(18), 2618–2631 (2021)
28. Ma, Y., Cao, W., Yang, L., F, T.L.M: Virtual synchronous generator control of full converter wind turbines with short-term energy storage. IEEE Trans. Ind. Electron. 64(11), 8821–8831 (2017)
29. Bajracharya, C., Molinas, M., Suul, J.A., Undeland, T.M.: Understanding of tuning techniques of converter controllers for VSC-HVDC. In: Nordic Workshop on Power and Industrial Electronics NORPIE, Helsinki, Finland (2008)
30. Yazdi, S.S.H., Fathi, S.H., Gharehpetian, G.B., EMa A.: Regulation of DC link voltage in VSC-HVDC to prevent DC voltage instability based on accurate dynamic model. In: 4th Power Electronics, Drive Systems and Technologies Conference (PEDSTC), Tehran, Iran, pp. 394–400 (2013)
31. Li, S., Wang, X., Yao, Z., Li, T., Peng, Z: Circulating current suppressing strategy for MMC-HVDC based on nonideal proportional resonant controllers under unbalanced grid conditions. IEEE Trans. Power Electron. 30(1), 387–397 (2015)
32. Rodríguez, P., Citro, C., Candela, J.I., Rocabert, J., Luna, A: Flexible grid connection and islanding of SPC-based PV power converters. IEEE Trans. Ind. Appl. 54(3), 2690–2702 (2018)
33. Pal, B., Chaudhuri, B, Robust Control in Power Systems. Vol. XXVI, p. 190 Springer, Boston, MA (2005)
34. Hu, J., Sun, L., Yuan, X., Wang, S., Chi, Y: Modeling of Type 3 wind turbines with df/dt inertia control for system frequency response study. IEEE Trans. Power Syst. 32(4), 2799–2809 (2017)
35. Anderson, P.M., Mirheydar, M: A low-order system frequency response model. IEEE Trans. Power Syst. 5(3), 720–729 (1990)
36. Mohseni, M., Islam, S.M: Review of international grid codes for wind power integration: Diversity, technology and a case for global standard. Renewable Sustainable Energy Rev. 16(6), 3876–3890 (2012)
37. Tan, Y., Muttaqi, K.M., Ciufo, P., Meegahapola, L: Enhanced frequency response strategy for a PMSG-based wind energy conversion system using ultracapacitor in remote area power supply systems. IEEE Trans. Ind. Appl. 53(1), 549–558 (2017)
38. Lee, J., Muljadi, E., Srensen, P., Kang, Y.C: Releasable kinetic energy-based inertial control of a DFIG wind power plant. IEEE Trans. Sustainable Energy 7(1), 279–288 (2016)


**How to cite this article:** Yazdi, S.S.H., Shokri-Kalandaragh, Y., Bagheri, M.: Power system stability improvement considering drive train oscillations of virtual synchronous generator-regulated type-4 wind turbines. IET Renew. Power Gener. 1–25 (2022). https://doi.org/10.1049/rpg2.12616

## APPENDIX A

Parameters of the 5 MW PMSG (Base values are its ratings):

Stator:$R_s = 0.0063$ p.u., $L_d = L_q = 0.3142$ p.u., $\lambda = 11.3658$ V.s, Pole pairs: $p = 148$, $P_N = 5$ MW, $U_N = 3$ kV, $\omega_{base} = 2 \times \pi \times 34.3$ rad/s, $i_s^{\max} = 1.08$ p.u., DC link: $C = 14000$ ¯F, $V_{DC}^* = 5940$ V, GSC:$L_i = 0.05$ p.u., $L_g = 0.0015$ p.u., $C_f = 0.05$ p.u., $R_f = 0.25$ p.u., $f_{SW} = 5$ kHz, $P_g^{\min} = 0$ p.u., Base grid frequency = 50 Hz.

Parameters of the 5 MW wind turbine (Base values are its ratings): $c_1 = 0.5$, $c_2 = 116$, $c_3 = 0.5$, $c_4 = c_5 = 0$, $c_6 = 0.5$, $c_7 = 21$, $c_8 = 0.08$, $c_9 = 0.035$, $\rho = 1.225$ kg/m$^3$ $\lambda^{\max} = 7.95$, $C_p^{\max} = 0.41$, Rated wind speed: 11.68 m/s, Cut-in wind speed: 6.83 m/s, Radius of WTG blades: 63 m, $H_t = 4.5$ s, $H_g = 0.6$ s, $K_{sh} = 1$ pu/elec.rad, $D_{tg} = 0.05$ p.u.

Parameters of the 75 MW thermal power plant (Base values are its ratings)

$\boldsymbol{R_{sg}} = 0.05$, $\boldsymbol{T_R} = 7\boldsymbol{s}$, $\boldsymbol{K_m} = 0.95$, $\boldsymbol{F_H} = 0.3$, $\boldsymbol{H_{sg}} = 5$, $\boldsymbol{D_{sg}} = 0.5$

Parameters of the energy storage system: $P_N = 1$ MW, $V_{DC}^N = 1800$ V, $V_{DC}^{Min} = 900$ V, $V_{DC}^* = 1423$ V, $C_{ESS} = 8.23$ F, $L_b = 0.3056$ mH, $ESR = 19.2$ mΩ, $|dV_{DC}/dt|_{\max} = 135$ V/s